

12837 Virtual Sensing of Offshore Wind Structures through Field Monitoring



Janina Branke

Pembroke College

University of Oxford

Supervisors: Manolis Chatziz and Daniel Powell

A report submitted in partial fulfilment
of the requirements for the degree of

Masters of Engineering Science

Trinity 2023

Abstract

This report focuses on improving the effective monitoring of various structures, such as offshore wind turbines, by leveraging accurate predictions of their structural dynamics. This predictive accuracy is critical to enhancing the life cycle of these structures, thus increasing revenue. To this end, we propose and thoroughly examine the use of an augmented Kalman filter to identify forces, system dynamics, and fatigue damage of an offshore wind turbine.

A finite element model is employed to characterise the wind turbine's structural dynamics and produce synthetic measurements for filter testing and tuning. The proficiency of the augmented Kalman filter is rigorously evaluated through a suite of tests that consider various aspects, such as the number of modes, sensor configurations, input forces, and the impact of model noise and parameter uncertainties. Both physical and modal coordinates are used for these tests.

This comprehensive analysis spans from modelling to practical applications, focusing on assessing the filter's performance under various conditions. The research findings suggest that the augmented Kalman filter can accurately predict the dynamics and fatigue life of an offshore wind turbine subjected to Kaimal loading using limited sensor measurements and without the need to measure the applied load. It is further shown that increasing the ratio of the process to measurement covariance noise is advantageous for real-world scenarios marked by modelling errors and more significant parameter uncertainties.

Acknowledgements

I would like to express my heartfelt gratitude to Manolis Chatzis and Daniel Powel for making this project possible through their invaluable guidance and support throughout. Both of you have been outstanding mentors, consistently taking the time to review my work and provide valuable feedback. Your expertise and encouragement have been essential to the completion of this project.

Thanks to Manolis's expertise and insights, I gained a deeper understanding of the underlying causes of the observations made during this project. Daniel's extensive knowledge and experience in the industry provided me with a unique perspective and helped me to understand how my work can be applied to real-world situations.

Thank you for your unwavering support and for helping me to grow as a researcher. I am deeply grateful for all that you have done for me.

Contents

1	Introduction	1
1.1	Motivation	2
2	Literature Review	3
2.1	Structural Health Monitoring	3
2.2	Input-State Estimation	4
3	Modelling	7
3.1	Synthetic Data Configuration	7
3.2	Reference Wind Turbine: IEA 15MW	7
3.2.1	OxDyn finite element modelling	8
3.2.2	System dynamics	9
3.2.3	Damping	11
3.2.4	Loading	12
3.2.4.1	Kaimal wind description	12
3.2.4.2	Jonswap wave description	12
3.2.5	Foundation	13
3.3	Modal Analysis	13
3.3.1	Modal truncation	14
3.4	Augmented Kalman filter	15
3.4.1	Filter tuning	17
3.5	Linear Observability	18
3.6	Fatigue Damage	19
3.6.1	S-N curve	20
4	Mass Spring Damper Results	23
4.1	System Description	23
4.2	Sensor Placement	24
5	Wind Turbine Results	27

5.1	Reference Scenario	27
5.2	Modal Truncation	29
5.3	Modal Forces	32
5.4	Offset	34
5.5	Sensor Placement	36
5.6	Loads Applied to the Wind Turbine	37
	5.6.1 Kaimal wind analysis	37
	5.6.2 Jonswap wave analysis	39
5.7	Noise and Uncertainties	40
5.8	Parameter Uncertainties	42
	5.8.1 Damping ratio	42
	5.8.2 Young's modulus and soil stiffness	43
6	Conclusion	45
6.1	Practical Conclusions	45
6.2	Recommendations for Further Work and Improvements	46

Chapter 1

Introduction

This report aims to evaluate the feasibility of employing an augmented Kalman filter (AKF) for predicting the dynamic response at unmeasured locations of an offshore wind turbine and estimating its fatigue life. Computational methods, including finite element analysis (FEM) and numerical modelling, are used to generate synthetic sensor measurements to demonstrate the AKF's potential. The AKF uses these measurements to estimate the kinematics, loads, and stresses within the structure, enabling the assessment of the wind turbine's structural health, which is especially valuable at critical locations which are typically challenging to measure, such as those underwater.

Section 2 presents a literature review on structural health monitoring, force identification, and fatigue damage assessment. This section offers a background on the current state of research in these areas and identifies the challenges and opportunities for further development. Section 3 delves into the modelling process to generate synthetic data, introducing the OxDyn Finite Element Modelling (FEM) framework and discussing the system dynamics, free vibration analysis, modal truncation, damping, and the implementation of the AKF.

The viability of the AKF is initially assessed by applying it to a simple mass-spring-damper system with two degrees of freedom in Section 4 to gauge the filter's responsiveness and accuracy. Additionally, the assumed covariance for the modelling and sensor noise are tuned and evaluated for their application in predicting system dynamics, as explained in Section 3.4.1.

Section 5 then applies the AKF to a comprehensive model of the National Renewable Energy Laboratory (NREL) 15MW wind turbine model [15] using 70 nodes. A realistic sensor setup is employed in this analysis, and practical considerations such as the sensors' quantity, type, and placement are considered while discussing the limitations of different sensor configurations. Moreover, different loading conditions, parameter uncertainties and noise levels are used to explore the AKF's feasibility in real-world applications. The time histories of the predicted states obtained from this analysis are used to identify the mudline stresses and estimate the wind turbine's fatigue life. In industry, the fatigue life of wind turbines is often estimated conservatively. By monitoring the accumulated fatigue damage

at critical locations within the structure, it becomes possible to safely extend the operational life of the wind turbine and generate additional income.

Section 6 concludes the report, summarising the findings, presenting practical conclusions based on this study's results, and offering potential extensions on the work.

1.1 Motivation

There is an urgent need for renewable energy sources, driven by the imperative to limit greenhouse gas emissions and foster energy independence. Offshore wind energy has become essential to the renewable energy mix, providing a clean and sustainable solution to the increasing energy demand. With some of Europe's most favourable offshore wind resources, the UK has emerged as a leading location for developing wind energy projects. Since the inception of the world's first offshore wind platform in 1991 [41], the UK has experienced rapid growth in wind energy. In 2009, the European Energy Directive 2009/28/EC set the target for the UK to meet 15% of its energy needs from renewable sources by 2020. Consequently, wind energy now constitutes 21% of the UK's current energy mix [16]. Offshore wind turbines have gained significant popularity compared to their onshore counterparts, primarily due to their higher energy returns and reduced concerns regarding noise and land displacement [26].

Many of the UK's wind turbines were designed with anticipated operational lifespans between 20 and 25 years [1]. As they approach the end of their intended service life, it becomes increasingly vital to prioritise their longevity. By closely monitoring the true dynamics of these structures, it is possible to use the sensor measurements to monitor stresses virtually. This information can then be directly used for fatigue analysis and better predict when the structure may reach the end of its safe operational period. Additional revenue can be generated by safely expanding the wind turbine's lifespan. For example, the 15 MW reference wind turbine discussed in this report generates an average annual energy production of 77.4 GWh [15]. Extending its life by just one year could yield an additional annual revenue of £26 million.

By implementing the AKF proposed in this report, it is possible to effectively monitor the dynamic response of offshore wind turbine structures at unmeasured locations. This approach can significantly contribute to the ongoing growth and success of the offshore sector by enhancing the system health monitoring processes. Moreover, the AKF not only provides advantages for managing structures such as wind turbines and bridges but can also be applied to a wide range of more general dynamic systems, including electrical, biological, and financial. For example, in aerospace navigation, the data from the Inertial Navigation System (INS) and the Global Positioning System (GPS) can be used to estimate the spacecraft's position, velocity, and orientation [34].

Chapter 2

Literature Review

2.1 Structural Health Monitoring

Structural Health Monitoring Systems (SHMS) can play a vital role in improving the capacity factor, maintenance costs, and sustainability of offshore wind turbines [7]. SHMS should include a network of sensors that monitor the dynamic responses of a structure and a data processing algorithm which infers its structural condition.

Within the framework of monitoring a structure's health, obtaining a chronological record of the forces exerted on the structure is very useful. When directly measuring these forces is challenging or unfeasible, it is necessary to deduce them indirectly. In the case of offshore structures, measuring all the environmental loads is impractical, given the structure's scale. The primary focus of the input identification problem is to reconstruct unmeasured forces by utilising response data collected from a limited number of sensors, along with a system model [28].

Civil engineering structures are subjected to continuous wear and tear, which can lead to fatigue and eventual failure. While a considerable body of research has focused on estimating structural or modal properties for several decades [45], much of this literature assumes that the excitation is either white noise or measured. However, knowing the parameters alone is insufficient for estimating fatigue without a clear understanding of the excitations. As a result, this report concentrates on input estimation, specifically virtual sensing, rather than parameter estimation. The states and input forces are estimated jointly by the AKF rather than relying on separate algorithms.

Virtual sensors present challenges due to uncertainty in environmental loads and dynamic characteristics. Addressing these challenges can significantly benefit the UK's low-carbon energy sector by enhancing profitability.

2.2 Input-State Estimation

The challenge of force identification typically involves reconstructing unmeasured dynamic forces acting on a structure by utilising its response, measured by a limited number of sensors and a system model. This system model can be obtained through a priori dynamic system identification. In scenarios where direct force measurements are difficult or impossible, it becomes necessary to determine excitation sources inversely. Inverse approaches for reconstructing these forces introduce uncertainty due to measurement errors in the recorded response and model errors in the modelling assumptions.

In the realm of structural dynamics, force identification problems were first addressed in the 1980s, employing frequency domain techniques [13]. However, numerous alternative methods have since been developed, primarily in the time domain and following a deterministic approach [47]. In recent years, there has been a shift towards combined deterministic-stochastic methods derived from control engineering. These methods differ from purely deterministic techniques by incorporating noise as a stochastic process and considering its presence in both measurements and state variables while treating unmeasured force values as deterministic quantities.

One of the first examples of combined deterministic-stochastic techniques to force estimation in structural dynamics was presented by Ma et al. [29], who used a Kalman filter in conjunction with a recursive least-squares estimator to estimate impulsive loads on a mass-spring-damper chain. Subsequently, successful force identification experiments on physical plates and beams in laboratories were reported, enabled by modelling these structures as single degree of freedom (SDOF) systems.

Lourens et al. [28] compare the use of the AKF to Dynamic Programming (DP) [37] to identify dynamic forces in a combination of deterministic and stochastic settings on a steel beam. In situations where it is possible to take measurements directly from the location of the force, the AKF outperformed the DP algorithm, as the AKF can incorporate modelling errors into the identification process. Their work demonstrated that results are significantly improved by increasing the number of sensors applied to the structure. A subsequent study by Van der Male and Lourens [46], demonstrated the ability to compensate for modelling errors on a lattice support structure.

State-space descriptions of systems problems typically involve both state and measurement equations. States are the generalised variables describing a first-order state space system, such as a vector comprising the degrees of freedom and their time derivatives. The measurement equation establishes the connection between the available sensor measurements and the internal states, whereas the state equation tracks the time evolution of the system's dynamic states [34]. The Kalman filter is an effective filter for state estimation when both the state equation and measurement equation are linear and subject to Gaussian noises [24]. It involves predicting the current states of the system based on the previous states and inputs and then updating these predictions based on the measurement data [3].

State estimation refers to estimating a system's internal states based on measurements of its inputs and

outputs. Parameter estimation, on the other hand, involves estimating the parameters that govern the behaviour of a system, such as its physical characteristics or environmental conditions. In the context of nonlinear systems, parameters can be added to an augmented state vector to describe the system in terms of a new, nonlinear augmented state vector.

Extensions of the Kalman filter to nonlinear systems include the unscented Kalman filter (UKF) and the extended Kalman filter (EKF). The UKF involves propagating a set of ‘sigma points’ through the nonlinear system dynamics and then using them to compute the mean and covariance of the state estimate to nonlinear systems [48]. The EKF is designed to handle nonlinear systems by linearising the system dynamics and measurement models around the current state estimate [40]. Both the UKF and EKF assume that all applied excitations to the system are measured. Meanwhile, in the case of a wind turbine, where excitations are not directly measured, the augmented Kalman filter (AKF) can be used to estimate the system states and forces. The system dynamics of the wind turbine explored in this report are linear. The AKF enhances the basic Kalman filter by incorporating additional states or parameters into the state vector, enabling the estimation of both system states and parameters simultaneously. The AKF can handle state-input estimation and can also be adapted to handle state-parameter-input estimation by simultaneously estimating the system states, parameters, and inputs in an extended state vector [11]. One limitation of the AKF is that it requires direct feedback in the measurement equation to identify an unmeasured force. This can be problematic when direct feedback is unavailable or difficult to obtain. However, this collocation condition required by the AKF is not unreasonable to satisfy for wind loads since there is typically a SCADA accelerometer at the nacelle. A more recently developed method for state and fatigue estimation with unknown forces is modal expansion, which has resulted in a high degree of accuracy when applied to jacket substructures [19].

The previously mentioned papers have provided valuable contributions to the methods and results utilised in this report. This report builds on the work of Laurens et al. [28] by exploring the AKF’s capabilities when applied to a wind turbine model. This project aims to implement all algorithms from scratch, including the implementation of the AKF. The AKF’s popularity as the most used input estimation algorithm, coupled with its simpler description compared to other advanced filtering techniques, is advantageous for this project. Furthermore, the AKF has been shown to give reasonable estimates for several applications, making it an interesting choice for investigating its applicability on a wind turbine (WT). While the properties of a wind turbine may not always be perfectly known, designers typically have reasonable estimates, and uncertainty can be accounted for or reduced through past structural health monitoring campaigns that achieve parameter estimation. Moreover, in the problem of fatigue estimation, the excitations often have much greater uncertainties than the structural parameters. In this application, the AKF is successful if it can identify the stresses at the root of the structure, even if the excitations are not estimated correctly. Furthermore, the AKF can provide better estimates for virtual sensors than the actual inputs by accounting for errors and enhancing state estimation, making it a valuable tool for stress estimation.

Using synthetic measurements generated by a finite element model, the stresses and excitation forces are inferred at critical locations which are difficult to monitor directly. A realistic subset of virtual sensors is used in this analysis. To evaluate the feasibility of using an AKF on a real wind turbine, realistic inputs such as Kaimal wind and Jonswap wave loading are evaluated. Moreover, the impact of noise and parameter uncertainties such as the damping ratio, Young's modulus and soil stiffness are explored.

Chapter 3

Modelling

3.1 Synthetic Data Configuration

Synthetic data refers to artificially generated data that mimics the characteristics of real-world data but does not contain any actual information from real-world observations. It allows the performance of the AKF to be evaluated quickly and cost-effectively. Introducing synthetic data with variations or noise can help ensure the robustness of the AKF by analysing the filter with a wide range of scenarios. In this report, the synthetic data used to evaluate the AKF is created using the OxDyn finite element model [31].

The model does not fully mirror the dynamics of a real wind turbine. However, the synthetic data reasonably reproduces the challenges when analysing data obtained from a real wind turbine. This means that the conclusions drawn from the synthetic data can be applied to physical wind turbines.

3.2 Reference Wind Turbine: IEA 15MW

The reference wind turbine used for the simulations in this report is the IEA 15MW reference wind turbine with a fixed-bottom support structure, as illustrated in Figure 3.1. The full wind turbine specifications, including the blade, rotor, tower, monopile, nacelle and drivetrain properties, are described in [15]. The reference wind turbine serves as a fundamental benchmark for research, development, and comparative analysis purposes.

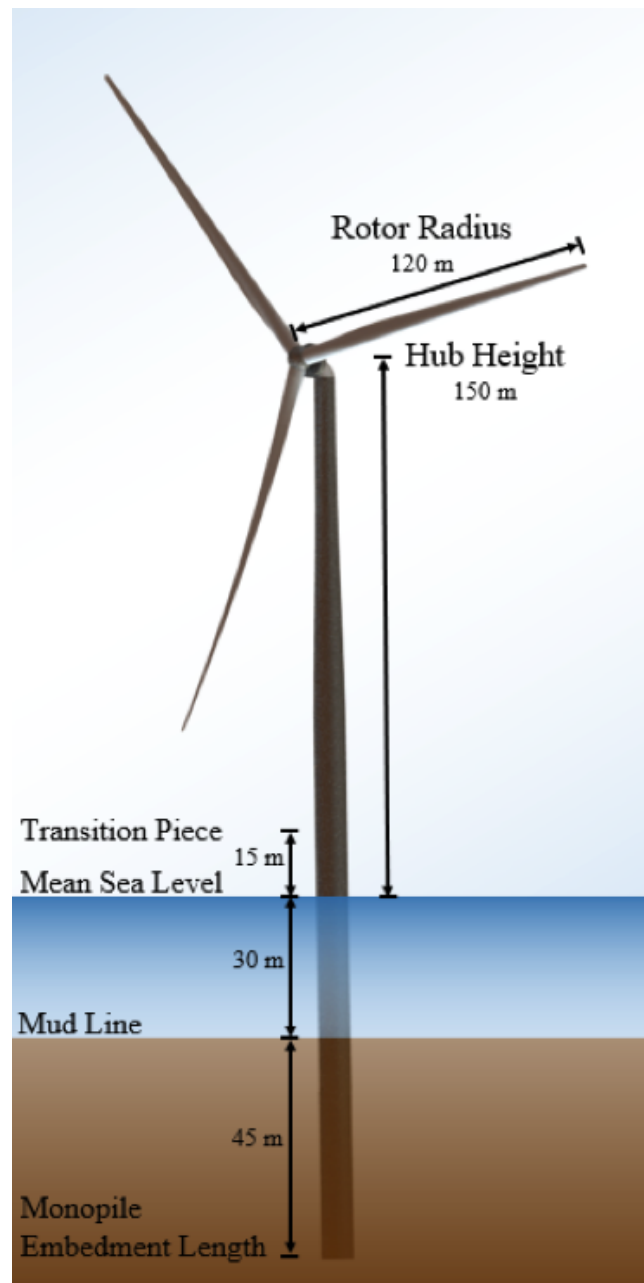


Figure 3.1: 15MW IEA reference wind turbine

3.2.1 OxDyn finite element modelling

Finite element analysis (FEA) [49] is used to analyse and solve complex engineering problems. It involves breaking down a physical structure or system into smaller, discrete parts, known as finite elements, and solving for the response of each of these elements.

Figure 3.2 shows an example of how FEA can be applied. The structure is discretised into a mesh, consisting of a set of interconnected elements, each representing a small region. The behaviour of each element is determined by solving a set of equations that describe the material's physical behaviour and the element's geometric shape. The results are combined to give an overall understanding of the behaviour of the entire structure or system.

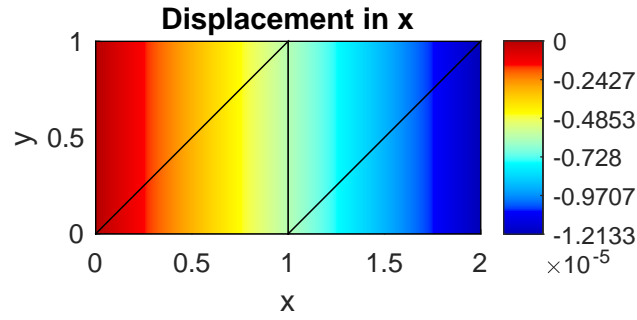


Figure 3.2: An example of FEA

For this report, the 1D FEA software OxDyn [31] is used to create the mesh and run the FEA for the wind turbine models. Variables of the system such as damping, foundation type, soil profile, scouring, stiffness, type of analysis and loading are taken into account. The initial conditions for the displacements and velocities for each degree of freedom are assumed to be zero. The pile-tower structure is modelled using twelve-degree-of-freedom Timoshenko beam elements [14]. Elements, where no Timoshenko beam properties (GA_κ and ϕ) have been assigned are treated as Euler-Bernoulli structural elements with zero shear stiffness (GA_κ) and bending to shear stiffness ratio (ϕ). The Timoshenko beam element is utilised for elements with mixed shear properties based on the sum of the shear stiffness (GA_κ) within the element. Section 3.2.2 explains how the dynamic equations of motions are integrated into the FEA.

In this report, the AKF incorporates components from OxDyn, such as the state-space matrices, ensuring a consistent underlying model despite differing software implementations. However, using the same underlying model may introduce model bias due to a failure to capture the full range of possible inputs or outputs and systematically favour certain outcomes over others. It is advisable to employ external datasets or independent evaluators to address potential biases to validate the model's performance in future experiments.

3.2.2 System dynamics

The general equation of motion for a space-discretised linear system is given by:

$$\mathbf{M}\ddot{\mathbf{v}}(t) + \mathbf{C}\dot{\mathbf{v}}(t) + \mathbf{K}\mathbf{v}(t) = \mathbf{F}(t), \quad (3.1)$$

where $\mathbf{M} \in \mathbb{R}^{n \times n}$ is the mass matrix, $\mathbf{C} \in \mathbb{R}^{n \times n}$ is the damping matrix and $\mathbf{K} \in \mathbb{R}^{n \times n}$ is the stiffness matrix, with n being the number of degrees of freedom. $\mathbf{v}(t) \in \mathbb{R}^n$ is the displacements vector and $\mathbf{F}(t) \in \mathbb{R}^n$ represents the force vector.

The Newmark time integration method [35] is used to incorporate the system dynamics from Equation 3.1 into the FEA to generate synthetic data. This method uses two parameters, β and γ , which control the numerical damping and accuracy. These are used in the Newmark equations to update

the displacement and velocity at each time step:

$$\mathbf{v}(t_{n+1}) = \mathbf{v}(t_n) + \Delta t \dot{\mathbf{v}}(t_n) + \left(\frac{1}{2} - \beta\right)(\Delta t)^2 a(t_n) + \beta(\Delta t)^2 \ddot{\mathbf{v}}(t_{n+1}) \quad (3.2)$$

$$\dot{\mathbf{v}}(t_{n+1}) = \dot{\mathbf{v}}(t_n) + (1 - \gamma)\Delta t \ddot{\mathbf{v}}(t_n) + \gamma\Delta t \ddot{\mathbf{v}}(t_{n+1}). \quad (3.3)$$

Next, accelerations at the next time step ($\ddot{\mathbf{v}}(t_{n+1})$) are found by rearranging the system equation and updating the force vector at each time step:

$$\ddot{\mathbf{v}}(t_{n+1}) = \mathbf{M}^{-1}(\mathbf{F}(t_{n+1}) - \mathbf{C}\dot{\mathbf{v}}(t_{n+1}) - \mathbf{K}\mathbf{v}(t_{n+1})). \quad (3.4)$$

This process is iterated through all time steps, updating the displacement, velocity and acceleration using the Newmark equations.

To find the continuous-time state-space representation of Equation 3.1, let:

$$\mathbf{x}(t) = \begin{bmatrix} \mathbf{v}(t) \\ \dot{\mathbf{v}}(t) \end{bmatrix}, \quad \text{and} \quad \mathbf{F}(t) = \mathbf{S}_f \mathbf{u}(t), \quad (3.5)$$

where \mathbf{S}_f is the load selection matrix. The matrices from the general equation of motion can be used to assemble the continuous system matrices $\mathbf{A}_c \in \mathbb{R}^{n_s \times n_s}$, $\mathbf{B}_c \in \mathbb{R}^{n_s \times n_s}$, $\mathbf{C}_c \in \mathbb{R}^{n_s \times n_s}$ and $\mathbf{D}_c \in \mathbb{R}^{n_s \times n_s}$.

$$\dot{\mathbf{x}}(t) = \mathbf{A}_c \mathbf{x}(t) + \mathbf{B}_c \mathbf{u}(t), \quad \mathbf{y}(t) = \mathbf{C}_c \mathbf{x}(t) + \mathbf{D}_c \mathbf{u}(t), \quad (3.6)$$

$$\mathbf{A}_c = \begin{bmatrix} \mathbf{0} & \mathbf{I} \\ -\mathbf{M}^{-1}\mathbf{K} & -\mathbf{M}^{-1}\mathbf{C} \end{bmatrix} \quad (3.7)$$

$$\mathbf{B}_c = \begin{bmatrix} \mathbf{0} \\ -\mathbf{M}^{-1}\mathbf{C} \end{bmatrix} \cdot \mathbf{S}_f \quad (3.8)$$

$$\mathbf{C}_c = \begin{bmatrix} \mathbf{S}_d & \mathbf{0} & \mathbf{0} \\ \mathbf{0} & \mathbf{S}_v & \mathbf{0} \\ \mathbf{0} & \mathbf{0} & \mathbf{S}_a \end{bmatrix} \cdot \begin{bmatrix} \mathbf{I} & \mathbf{0} \\ \mathbf{0} & \mathbf{I} \\ \mathbf{M}^{-1}\mathbf{K} & \mathbf{M}^{-1}\mathbf{C} \end{bmatrix} \quad (3.9)$$

$$\mathbf{D}_c = \begin{bmatrix} \mathbf{S}_d & \mathbf{0} & \mathbf{0} \\ \mathbf{0} & \mathbf{S}_v & \mathbf{0} \\ \mathbf{0} & \mathbf{0} & \mathbf{S}_a \end{bmatrix} \cdot \begin{bmatrix} \mathbf{0} \\ \mathbf{0} \\ \mathbf{M}^{-1} \end{bmatrix}, \quad (3.10)$$

where \mathbf{S}_d , \mathbf{S}_v and \mathbf{S}_a are the selection matrices for displacement, velocity and acceleration sensors, respectively. The model order, denoted as n_s , refers to the number of state variables necessary to

describe the system's dynamics. For this particular system, the model order is equal to two times the value of n .

The AKF requires a description of the system in discrete time form, so the continuous state space matrices are discretised assuming a zero-order-hold is applied to the system inputs:

$$\mathbf{A}_d = \exp(\mathbf{A}_c \Delta t), \quad \mathbf{B}_d = [\exp(\mathbf{A}_c \Delta t) - \mathbf{I}] \mathbf{A}_c^{-1} \mathbf{B}_c \quad (3.11)$$

$$\mathbf{C}_d = \mathbf{C}_c, \quad \mathbf{D}_d = \mathbf{D}_c, \quad (3.12)$$

The discretised state space model can be expressed as:

$$\mathbf{x}_{k+1} = \mathbf{A}_d \mathbf{x}_k + \mathbf{B}_d \mathbf{u}_k + \mathbf{w}_k \quad (3.13)$$

$$\mathbf{y}_k = \mathbf{C}_d \mathbf{x}_k + \mathbf{D}_d \mathbf{u}_k + \mathbf{v}_k. \quad (3.14)$$

Note that the subscripts c and d are used to label the continuous and discrete matrices, respectively. To account for process modelling and measurement noise, the state space equation in discrete time is augmented with the random noise variables $\mathbf{w}_k \in \mathbb{R}^{n_s}$ and $\mathbf{v}_k \in \mathbb{R}^{n_d}$ which represent the process and measurement noises, respectively. They are assumed to be zero-mean, independent random processes.

3.2.3 Damping

To create the damping matrix (\mathbf{C}) in the physical coordinates, it is assumed to be proportional to the mass (\mathbf{M}) and stiffness (\mathbf{K}) matrices, as follows:

$$\mathbf{C} = \alpha \mathbf{M} + \beta \mathbf{K}, \quad (3.15)$$

transformed into modal coordinates, this becomes:

$$\mathbf{C}^* = \alpha \mathbf{M}^* + \beta \mathbf{K}^*. \quad (3.16)$$

For a single degree of freedom (SDOF) system, the damping coefficient (c) can be expressed in terms of the damping ratio (ζ), mass (m), and natural frequency (ω) as:

$$c = 2m\zeta\omega. \quad (3.17)$$

In the modal coordinates, this relationship can be extended to the modal damping matrix, where the mass is from the diagonalised mass matrix, \mathbf{M}^* and ω is the natural frequency for that mode.

3.2.4 Loading

The loads on an offshore wind turbine can be categorised into two main types: static loads and dynamic loads, both of which contribute to the fatigue life. Static loads comprise the weight of the turbine, the weight of the tower, and the tension in the cables that anchor the turbine to the seabed. Examples of dynamic loads include the wind loads, wave loads and the loads induced by the rotating turbine blades. This report analyses the AKF's ability to monitor both wind and wave loading, as these are the most significant loading sources. The Kaimal wind loading is a realistic approximation of wind loading, recommended by the International Electrotechnical Commission (IEC) wind turbine design standard [8], and Jonswap wave loading is a well-established and widely used standard in the offshore industry [17].

3.2.4.1 Kaimal wind description

The auto-spectral density suggested by Kaimal et al. [23] is characterised by a power-law behaviour, with the wind speed at each frequency following a particular distribution. The spectrum is typically expressed in terms of the mean wind speed (u) and the standard deviation of the wind speed (σ). The Kaimal spectrum can be used to estimate the wind loads on a structure by calculating the mean wind speed and standard deviation at each point on the structure and using these values to determine the wind loads. This equation to describe the load spectrum is given by the international standard IEC 61400 [21] as:

$$S(f) = \sigma^2 \frac{4fL_k/V_{mean}}{(1 + 6fL_k/V_{mean})^{5/3}}. \quad (3.18)$$

Figures of the force and displacement time-histories for an applied Kaimal wind are shown in Section 5.6.1.

3.2.4.2 Jonswap wave description

Wave kinematics are typically calculated based on the guidelines outlined in IEC 61400-3-1 [9], an international wind turbine standard.

JONSWAP [18] (Joint North Sea Wave Project) is a wave spectrum model that describes the sea wave conditions in the North Sea. It is defined as the normalised wave spectrum that describes the distribution of wave energy as a function of frequency and wave height.

$$S(f) = \alpha g^2 f^{-5} \exp^{-(f/f_p)^4} \gamma^\beta, \quad (3.19)$$

where

$$\beta = \exp\left[-\frac{1}{2\sigma^2} \left(\frac{f}{f_m} - 1\right)^2\right] \quad (3.20)$$

$$\sigma = \begin{cases} \sigma_1 & \text{for } f \leq f_m \\ \sigma_2 & \text{for } f > f_m. \end{cases} \quad (3.21)$$

Here, g is the acceleration due to gravity, f is the frequency, f_p is the peak frequency and γ , α , σ_1 and σ_2 are data points given in [2]. Note that the Jonswap wave loading acts on all sub sea-level nodes. The Jonswap wave loading will be evaluated on an offshore wind turbine in Section 5.6.2, where figures of the force and corresponding displacement time histories are presented.

3.2.5 Foundation

The PISA (Pile Soil Analysis) project is a research initiative aimed at developing design methods for monopile foundations in offshore wind turbine structures. In this report PISA Cowden clay [6], a type of soft clay commonly found in offshore environments, is used. The PISA design model is helpful for various practical design calculations, including determining small displacement foundation stiffness for dynamic modelling, analysing serviceability limit states for normal working conditions, and analysing ultimate limit states for overall stability [5]. Offshore wind turbines are adapted to each site's specific conditions and requirements. Various support structures, including monopiles, gravity foundations, tripods, jackets, suction buckets, or tension legs, can be utilised by seabed-attached wind turbines [42]. The IEA 15MW wind turbine used in this report has a monopile foundation, similar to around 80.5% [39] of European offshore wind turbines.

3.3 Modal Analysis

Natural frequencies, also known as eigenfrequencies or resonant frequencies, are frequencies at which a system will resonate when subjected to an external broadband excitation.

For an undamped system, $\mathbf{M}\ddot{\mathbf{v}} + \mathbf{K}\mathbf{v} = \mathbf{0}$, it is possible to substitute the general form of \mathbf{v} as $\mathbf{v} = \boldsymbol{\psi} \sin \omega t$, giving $(\mathbf{K} - \omega^2 \mathbf{M})\boldsymbol{\psi} = \mathbf{0}$, and $\det(\mathbf{K} - \omega^2 \mathbf{M}) = 0$.

From the above equations, the natural frequencies are given by the roots of $\mathbf{M}^{-1}\mathbf{K}$ and the modeshapes are given by the respective eigenvectors.

The matrix of eigenvectors $\mathbf{V} \in \mathbb{R}^{n \times n}$ and the diagonal matrix of eigenvalues $\boldsymbol{\Lambda}$ are given by:

$$\mathbf{V} = [\mathbf{V}_1 \mathbf{V}_2 \dots \mathbf{V}_n] \quad \text{and} \quad \boldsymbol{\Lambda} = [\omega^2]. \quad (3.22)$$

To uncouple the system equations, it is possible to use the method of modal coordinates, expressing the generalised coordinates and velocities in terms of a set of modal coordinates and velocities, as follows:

$$\mathbf{v} = \mathbf{V}\mathbf{X} \quad (3.23)$$

$$\dot{\mathbf{v}} = \mathbf{V}\dot{\mathbf{X}}. \quad (3.24)$$

The linear response of a system can be expressed in terms of its mode shapes:

$$\mathbf{v}(t) = \psi_1\mathbf{X}_1(t) + \psi_2\mathbf{X}_2(t) + \dots + \psi_n\mathbf{X}_n(t). \quad (3.25)$$

Substituting \mathbf{X} into the general equation of motion, given by Equation 3.1 and multiplying through by \mathbf{V}^T gives:

$$\mathbf{V}^T\mathbf{M}\mathbf{V}\ddot{\mathbf{X}} + \mathbf{V}^T\mathbf{C}\mathbf{V}\dot{\mathbf{X}} + \mathbf{V}^T\mathbf{K}\mathbf{V}\mathbf{X} = \mathbf{V}^T\mathbf{F}(t). \quad (3.26)$$

This equation can be rewritten as:

$$\mathbf{M}^*\ddot{\mathbf{X}} + \mathbf{C}^*\dot{\mathbf{X}} + \mathbf{K}^*\mathbf{X} = \mathbf{F}^*(t), \quad (3.27)$$

where \mathbf{M}^* , \mathbf{C}^* , and \mathbf{K}^* are the modal mass, damping, and stiffness matrices, respectively, and \mathbf{F}^* is the modal force vector.

By using modal coordinates, the original equations of motion have been converted into a set of decoupled equations, one for each mode. This allows the dynamic response to be analysed more easily by treating each modal coordinate separately. Once the modal displacements and velocities have been found, they can be transformed back to the original coordinates and velocities using the inverse transformation.

3.3.1 Modal truncation

In many engineering structures, the applied loads contain mostly low-frequency content, meaning that modal truncation dramatically reduces the complexity and processing times for the system while retaining most of the information. Modal truncation is a technique used to approximate the behaviour of a linear dynamic system by retaining only a limited number of its characteristic modes, or natural frequencies and corresponding modes of vibration.

In wind turbine systems, vibrations occur due to the dynamic loading of the blades, tower, and other components. These vibrations can be categorised based on their frequency, and different frequency ranges can affect the system's overall behaviour differently. In general, the low-frequency modes of vibration in wind turbine systems are considered the most important for determining the system's overall behaviour. These vibrations typically occur below 1 Hz and are mainly caused by wind turbulence, tower shadow, and blade-passing frequencies. The low-frequency vibrations can cause structural deformations and fatigue damage to the components, affecting the overall performance and lifespan

of the turbine. On the other hand, high-frequency modes of vibration in wind turbine systems are mainly caused by blade structural modes, turbulence-induced vibrations, and electrical interactions. While high-frequency vibrations can also cause damage to the components, they are generally less significant in determining the system's overall behaviour than low-frequency modes.

The matrices $\mathbf{A}_c \in \mathbb{R}^{2n_m \times 2n_m}$, $\mathbf{B}_c \in \mathbb{R}^{2n_m \times n_p}$, $\mathbf{G}_c \in \mathbb{R}^{n_d \times 2n_m}$ and $\mathbf{J}_c \in \mathbb{R}^{n_d \times n_p}$ from Equations 3.7 and 3.9 can be rewritten in terms of its mass normalised modal coordinates $\phi \in \mathbb{R}^{n_{dof} \times n_m}$ and $\mathbf{\Omega} \in \mathbb{R}^{n_m \times n_m}$, containing the system's natural frequencies ω_i along the diagonal. The modal damping matrix $\mathbf{\Gamma} \in \mathbb{R}^{n_m \times n_m}$ is a diagonal matrix, with the terms $2\xi_i\omega_i$ along its diagonal where ξ is the modal damping ratio. Here, n_m , n_p , n_d , n_{dof} denote the number of modal coordinates, input forces, measured nodes and degrees of freedom, respectively.

$$\mathbf{A}_c = \begin{bmatrix} \mathbf{0} & \mathbf{I} \\ -\mathbf{\Omega}^2 & -\mathbf{\Gamma} \end{bmatrix}, \quad \mathbf{B}_c = \begin{bmatrix} \mathbf{0} \\ \phi^T \end{bmatrix} \quad (3.28)$$

$$\mathbf{G}_c = \begin{bmatrix} \phi & \mathbf{0} \\ \mathbf{0} & \phi \\ \phi\mathbf{\Omega}^2 & \phi\mathbf{\Gamma} \end{bmatrix}, \quad \mathbf{J}_c = \begin{bmatrix} \mathbf{0} \\ \mathbf{0} \\ \phi\phi^T \end{bmatrix}. \quad (3.29)$$

This results in the equivalent discrete-time state-space model:

$$\zeta_{k+1} = \mathbf{A}\zeta_k + \mathbf{B}p_k\mathbf{d}_k = \mathbf{G}\zeta_k + \mathbf{J}p_k, \quad (3.30)$$

where $\zeta_k = \zeta(k\Delta t)$ and $\mathbf{p}_k = \mathbf{p}(k\Delta t)$ for $k = 1, \dots, N$.

3.4 Augmented Kalman filter

An augmented Kalman filter is a type of recursive state estimator that can be used to estimate the state of a system based on noisy measurements. It is an extension of the standard Kalman filter that allows for the incorporation of additional variables, known as augmented variables, into the state estimate.

The basic idea behind an augmented Kalman filter is to use a mathematical model of the system and a set of noisy measurements to estimate the system's state and applied inputs at each time step. The filter uses a prediction step to estimate the system's state at the next time step, based on the current state and the system dynamics, and a correction step to refine the estimate based on the measurements. The Kalman gain, which reflects the relative weight of the measurements and the predictions, is used to determine how much the measurements should influence the state estimate.

The augmented state equation is formulated as:

$$\mathbf{x}_{\mathbf{k}+1}^{\mathbf{a}} = \mathbf{A}_{\mathbf{a}}\mathbf{x}_{\mathbf{k}}^{\mathbf{a}} + \zeta_{\mathbf{k}}, \quad (3.31)$$

and the augmented observation equation becomes:

$$\mathbf{y}_{\mathbf{k}} = \mathbf{G}_{\mathbf{a}}\mathbf{x}_{\mathbf{k}}^{\mathbf{a}} + v_{\mathbf{k}}. \quad (3.32)$$

The augmented state-space model is derived from the discrete-time state, given by Equation 3.13.

The time variation of the force is given by:

$$\mathbf{u}_{\mathbf{k}+1} = \mathbf{u}_{\mathbf{k}}\eta. \quad (3.33)$$

The augmented state vector $\mathbf{x}_{\mathbf{k}}^{\mathbf{a}}$ and noise vector $\zeta_{\mathbf{k}}$ are defined as follows:

$$\mathbf{x}_{\mathbf{k}}^{\mathbf{a}} = \begin{bmatrix} \mathbf{x}_{\mathbf{k}} \\ \mathbf{u}_{\mathbf{k}} \end{bmatrix}, \quad \zeta_{\mathbf{k}} = \begin{bmatrix} \mathbf{w}_{\mathbf{k}} \\ \eta_{\mathbf{k}} \end{bmatrix}, \quad (3.34)$$

where $\zeta \in \mathbb{R}^{n_p}$ refers to the force noise variable. The augmented system matrices are of the form:

$$\mathbf{A}_{\mathbf{a}} = \begin{bmatrix} \mathbf{A} & \mathbf{B} \\ \mathbf{0} & \mathbf{I} \end{bmatrix}, \quad \mathbf{G}_{\mathbf{a}} = \begin{bmatrix} \mathbf{C} & \mathbf{D} \end{bmatrix}, \quad (3.35)$$

where the matrices \mathbf{A} , \mathbf{B} , \mathbf{C} and \mathbf{D} are the discretised state matrices derived in Equations 3.11 and 3.12. The AKF also takes into account the independent process noise, $\mathbf{w}_{\mathbf{k}}$, measurement noise, $\mathbf{v}_{\mathbf{k}}$, and force increment $\eta_{\mathbf{k}}$. Their covariance matrices are represented by $\mathbf{Q} \in \mathbb{R}^{n_s \times n_s}$, $\mathbf{R} \in \mathbb{R}^{n_d \times n_d}$ and $\mathbf{S} \in \mathbb{R}^{n_p \times n_p}$, respectively. The distributions of $\mathbf{w}_{\mathbf{k}}$, $\mathbf{v}_{\mathbf{k}}$ and $\zeta_{\mathbf{k}}$ are given by:

$$p(\mathbf{w}) \sim N(0, \mathbf{Q}) \quad (3.36)$$

$$p(\mathbf{v}) \sim N(0, \mathbf{R}) \quad (3.37)$$

$$p(\eta) \sim N(0, \mathbf{S}). \quad (3.38)$$

The AKF estimates the augmented state vector, $\hat{\mathbf{x}}_{\mathbf{k}}$ of the system through iterative updating. The measurement update of the AKF incorporates new measurements by updating the Kalman gain $\mathbf{L}_{\mathbf{k}}$, which is used to compute an updated state estimate using the measurements $\mathbf{d}_{\mathbf{k}}$. Next, the error covariance noise $\mathbf{P}_{\mathbf{k}|\mathbf{k}}$ is updated, and the time update projects the state and error covariance matrix ahead.

The AKF's discrete time formulation [50] is:

1) Measurement update

$$\mathbf{L}_k = \mathbf{P}_{k|k-1} \mathbf{G}_a^T / (\mathbf{G}_a \mathbf{P}_{k|k-1} \mathbf{G}_a^T + \mathbf{R}) \quad (3.39)$$

$$\hat{\mathbf{x}}_{k|k} = \hat{\mathbf{x}}_{k|k-1} + \mathbf{L}_k (\mathbf{d}_k - \mathbf{G}_a \hat{\mathbf{x}}_{k|k-1}) \quad (3.40)$$

$$\mathbf{P}_{k|k} = \mathbf{P}_{k|k-1} - \mathbf{L}_k \mathbf{G}_a \mathbf{P}_{k|k-1}, \quad (3.41)$$

2) Time update

$$\hat{\mathbf{x}}_{k+1|k} = \mathbf{A}_a \hat{\mathbf{x}}_{k|k} \quad (3.42)$$

$$\mathbf{P}_{k+1|k} = \mathbf{A}_a \mathbf{P}_{k|k} \mathbf{A}_a^T + \mathbf{Q}_a, \quad (3.43)$$

where the augmented covariance matrix $\mathbf{Q}_a \in \mathbb{R}^{(n_s \times n_p) \times (n_s \times n_p)}$ is configured as follows:

$$\mathbf{Q}_a = \begin{bmatrix} \mathbf{Q} & \mathbf{0} \\ \mathbf{0} & \mathbf{S} \end{bmatrix}, \quad (3.44)$$

and the error covariance matrix is characterised by

$$\mathbf{P}_k = E \left[(x_k - \hat{x}_k)(x_k - \hat{x}_k)^T \right]. \quad (3.45)$$

The covariance matrices are diagonal due to the assumption that the uncertainties in the state variables are uncorrelated. The choice of these values along the diagonal of the \mathbf{Q}_a and \mathbf{R} matrices should take into consideration the order of magnitude of the state vector and the accuracy of the sensors, respectively.

In addition, the AKF is sensitive to the covariance matrix of the initial state error $\mathbf{P}_{0|0}$, which needs to be specified by the user but is typically unknown. In most cases, it is sufficient to assign very large values to the diagonal of this matrix. This has the effect of treating the initial errors as large and causing the filter to ignore the initial estimations, which can help to improve the accuracy of the AKF [28].

3.4.1 Filter tuning

The AKF uses measurement data to update its prediction at each time step and its performance can be improved by adjusting its parameters through a tuning process to account for the sensor and model uncertainties. To tune the filter, the model is run repeatedly for different process and measurement covariance matrices, as well as initial state estimation error matrices.

The process noise covariance matrix \mathbf{Q} characterises the uncertainty in the state space equations, encompassing both the inherent variability of the system and the assumptions made about its param-

eters. By adjusting the values of this matrix, the filter's ability to track the system state and respond to changes in the system can be controlled. Increasing the covariance noise means that the AKF will trust the system dynamics less, therefore relying more on the sensors. This will cause the AKF to make more accurate predictions on states that are close to the ones being measured, sometimes at the expense of other states, as shown in Section 4. In the wind turbine model used in this report, sensors are generally more reliable and their noise is very small. The measurement noise covariance matrix represents the uncertainty in the measurements being used to update the filter [4]. By tuning the values in the process noise covariance matrix, the filter's capacity to balance measurements in relation to the predicted state can be adjusted. This enables the AKF to account for different sensor types and variations in the measurement capabilities of the same type sensors at distinct locations. Increasing the process noise covariance matrix allows the AKF to be more robust to modelling errors whereas decreasing it can help to reduce the filter's sensitivity to measurement noise.

In the case that modal analysis is used, as explained in Section 3.3, the modal forces are used in place of physical forces. This serves as a more precise representation of the system dynamics, capturing the collective effect of the force on all points of a mode. Thus, the model's ability to accurately represent the true system behaviour is improved. This should be reflected in the process noise, which should be reduced to reflect the increased certainty in the process model.

To assess the accuracy of the AKF, the normalised error between the actual and predicted dynamics was initially employed. However, due to the possibility of obtaining large outputs for results close to zero, the use of R-squared difference, which represents the proportion of variance in the dependent variable that can be explained by the independent variable(s), was deemed more appropriate in this context. The equation for the R-squared is given by:

$$R^2 = 1 - \frac{\sum_{i=1}^n (y_i - \hat{y}_i)^2}{\sum_{i=1}^n (y_i - \bar{y})^2}, \quad (3.46)$$

where n is the number of observations, y_i is the observed value of the dependent variable for observation i , \hat{y}_i is the predicted value of the dependent variable for observation i and \bar{y} is the mean value of the dependent variable.

R-squared values are used throughout this report to provide a quantitative measure of the goodness of fit between the data and the predictions. In contrast, time histories only provide a visual representation of the data. A higher R-squared value indicates a better fit between the model and the data.

3.5 Linear Observability

Observability is a fundamental characteristic of dynamic systems used to determine whether it is theoretically possible to infer the system's internal state from its external outputs. The observability matrix is a tool used to evaluate the observability of a system, which is either subjected to measured

inputs or autonomous.

For a linear time-invariant system with state equation:

$$\dot{\mathbf{x}} = \mathbf{A}\mathbf{x} + \mathbf{B}\mathbf{u} \quad (3.47)$$

$$\mathbf{y} = \mathbf{C}\mathbf{x} + \mathbf{D}\mathbf{u}, \quad (3.48)$$

where \mathbf{x} is the state vector, \mathbf{u} is the input force, \mathbf{y} is the output, \mathbf{A} , \mathbf{B} , \mathbf{C} , and \mathbf{D} are constant matrices, and t is time, the observability matrix is in the form [20]:

$$\mathbf{O} = \begin{bmatrix} \mathbf{C}_d \\ \mathbf{C}_d\mathbf{A}_d \\ \mathbf{C}_d\mathbf{A}_d^2 \\ \dots \\ \mathbf{C}_d * \mathbf{A}_d^{n-1} \end{bmatrix}. \quad (3.49)$$

The observability matrix, \mathbf{O} , requires that the inputs to the system are known and must be full rank for the system to be observable. However, if the inputs are unknown, as for the offshore wind turbine explored in this report, the observability matrix of 3.49 is only part of the overall observability matrix. Maes, Chatzis and Lombaert indicate that the Observability Rank Condition for systems with Direct Feedthrough (ORC-DF) needs to be considered instead [30]. If the system is unobservable under measured inputs, it will remain unobservable if these inputs are considered unmeasured.

3.6 Fatigue Damage

This report aims to evaluate the fatigue within the structure to extend its life cycle. By evaluating the accuracy of the fatigue life estimate, it is possible to quantify how applicable this method is for extending the operational life of wind turbines. An accuracy of the fatigue life estimate of more than 95% is excellent. It is possible to greatly extend the life by showing that stresses are lower than anticipated at design. Therefore, it is not necessary to ever identify the correct force as long as the identified stress level and fatigue life are correct. Preexisting cracks and discontinuities affect the fatigue damage of offshore wind structures. Fatigue occurs when cyclical loading leads to the initiation and propagation of cracks within the structure [33].

The fatigue damage for the wind turbine is calculated at the mudline for the true and predicted signal, as there is a high stress concentration there. Internal section forces and properties at the structure's base are used to find the fatigue damage. It is not possible to place stress sensors at the mudline directly because this location is underwater and very difficult to access. Moreover, for sensors placed

below the ground level, the data quality is usually poor because the sensors are damaged during the installation process when the monopile is driven into the ground.

Figure 3.3 illustrates an example of the stress time history at the mudline when Kaimal wind is applied.

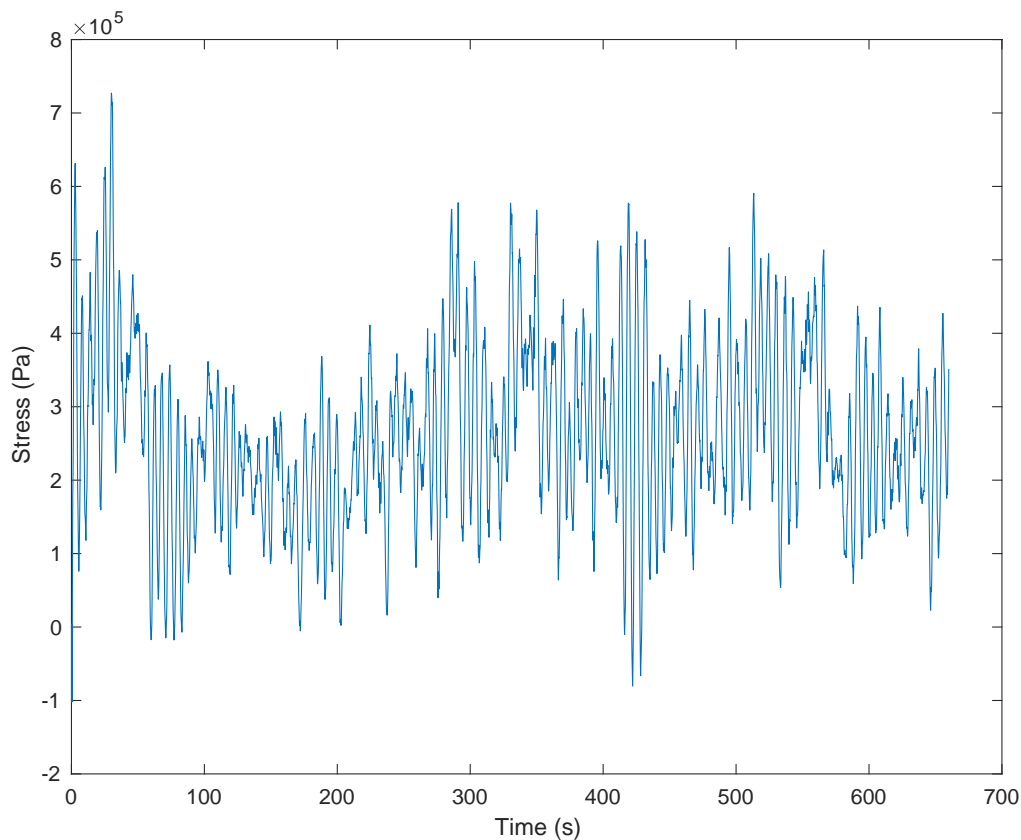


Figure 3.3: Example of stress time history

The stress's rainflow cycles are calculated from the internal stress time-history data in Figure 3.3 using Matlab's `rainflow()` function. The peaks and valleys in the time-history data are grouped into cycles, and the number of cycles and their magnitudes are tabulated. Rainflow counting registers each successive valley and peak as a separate cycle. Note that each response is only measured for 11 minutes, and rainflow counting might generate significantly different results between runs. For this reason, each simulation is run 20 times to find a reliable average rainflow result. Figure 3.4 shows a histogram of cycle counts as a function of stress range, obtained by applying the `rainflow()` function to the stress time-history from Figure 3.3.

Next, the equivalent stress amplitudes in each cycle is calculated using an S-N curve, which is used to find the damage to the structure.

3.6.1 S-N curve

The fatigue life of a structure describes the number of stress cycles a material can withstand before failure occurs due to fatigue. The fatigue design of offshore steel structures recommended practice

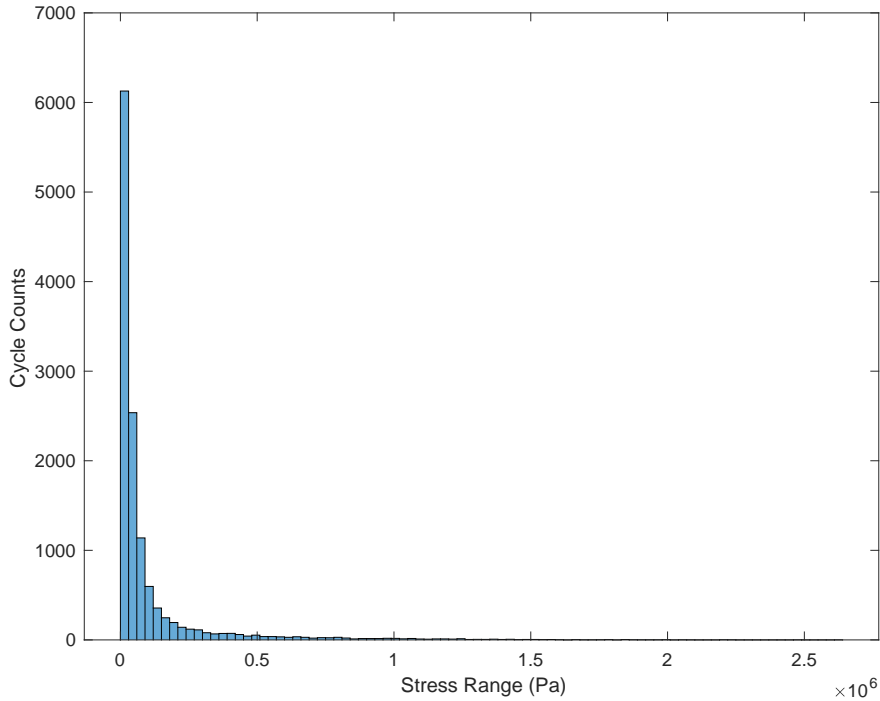


Figure 3.4: Histogram of cycle counts as a function of stress range

RP-C203 [12] is used to estimate fatigue life. The analysis uses the S-N curve for a double-sided circumferential weld with cathodic protection in seawater, which would be a typical governing fatigue detail near the mudline. The S-N curve equation is a mathematical model used to describe the relationship between the stress level and the number of cycles to failure of a material:

$$\log N = \log \bar{a} - m \log(\Delta\sigma), \quad (3.50)$$

where N is the predicted number of cycles to failure, $\log \bar{a}$ is the logarithm of the material's endurance limit, m is the slope of the S-N curve, determined by the material's properties and the loading conditions, and $\Delta\sigma$ is the stress amplitude of the cyclic loading. The values of m and $\log \bar{a}$ for the S-N curves in seawater with cathodic protection are 5 and 15.350, respectively [12].

The plate thickness influences the fatigue strength of welded joints as the stresses build up at the joints. The thickness effect can be accounted for by modifying the stress range for thicknesses larger than the reference thickness, which creates the modified design S-N curve:

$$\log N = \log \bar{a} - m \log \left(\Delta\sigma \left(\frac{t}{t_{ref}} \right)^k \right), \quad (3.51)$$

where k is the fatigue strength thickness exponent and t_{ref} is the reference thickness for the joint, as given by the DNV recommended practice.

In a real wind turbine, joints are subject to axial and bending stresses. The axial stresses, in this case, are significant because the Rotor and Nacelle Mass (RNA mass) have a combined weight of 1.02×10^6

kg. The longitudinal stress within the structure is therefore defined by:

$$\sigma_{total} = \frac{Force}{Area} + \frac{My}{I}. \quad (3.52)$$

The Palmgren-Miner rule [25] is used to estimate the damage fraction, C, as follows:

$$\sum_i \frac{n_i}{N_i} = C, \quad (3.53)$$

where N_i is the number of cycles to failure and n_i is the number of cycles completed at each stress level. The structure is predicted to fail at the time when the damage fraction C is equal to one.

Chapter 4

Mass Spring Damper Results

This report demonstrates two examples of the use of the AKF. The first example is shown in this chapter and focuses on a simplified two-degree-of-freedom mass-spring-damper system. The next chapter will apply the AKF to a complete wind turbine system.

4.1 System Description

To demonstrate the method and validate the coded algorithm of the AKF proposed by Lourens et al. [28], a simple two-degree-of-freedom (DoF) mass-spring-damper (MSD) system was set up as shown in Figure 4.1. It is easier to understand the effects of the AKF for this more straightforward system.

The system shown in Figure 4.1 consists of two masses, m_1 and m_2 , connected by springs k_1 and k_2 and dampers c_1 and c_2 . A force F is applied to m_2 in the direction of x_2 . The system's dynamic states describe the temporal evolution of the system. They are the displacements and velocities (v and \dot{v} respectively) of the two masses.

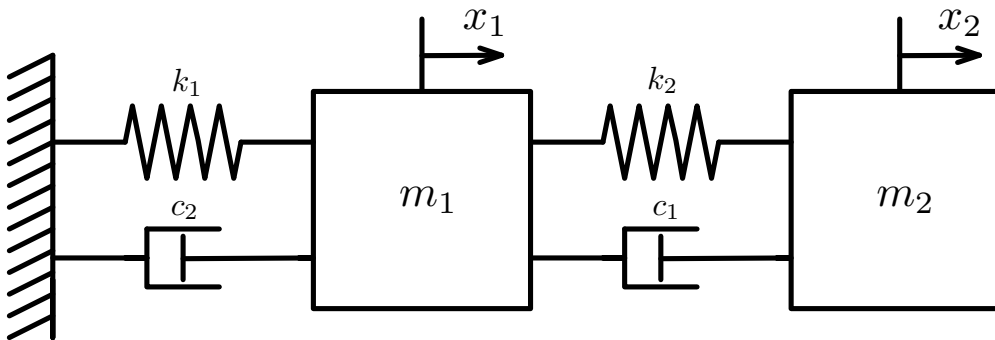


Figure 4.1: Two DoF Mass-Spring-Damper system

The masses m_1 and m_2 are 30,000 kg, the stiffness of springs k_1 and k_2 are 3kNm^{-1} , and the damping ratio for both modes is set to 1% to closely mimic an offshore wind turbine's dynamics [22]. In the following lines, a triangular pulse impulse is evaluated. The input and output sampling rate is 1000

Hz to capture the system's complete response.

The AKF uses covariance matrices \mathbf{R} , \mathbf{Q} and \mathbf{S} , which describe the uncertainty in the measurement vectors and estimated states. The discretised system matrices \mathbf{A}_d and \mathbf{G}_d in the AKF have been described in Section 3.4. Six possible sensors could be applied to this structure: one displacement, one velocity, and one acceleration sensor at each of the two degrees of freedom. The initial conditions are assumed to be zero.

4.2 Sensor Placement

This section explores a variety of sensor setups. A base case is established for the system by evaluating its performance when all sensors are used to update the AKF. The corresponding time histories are shown in Figure 4.2.

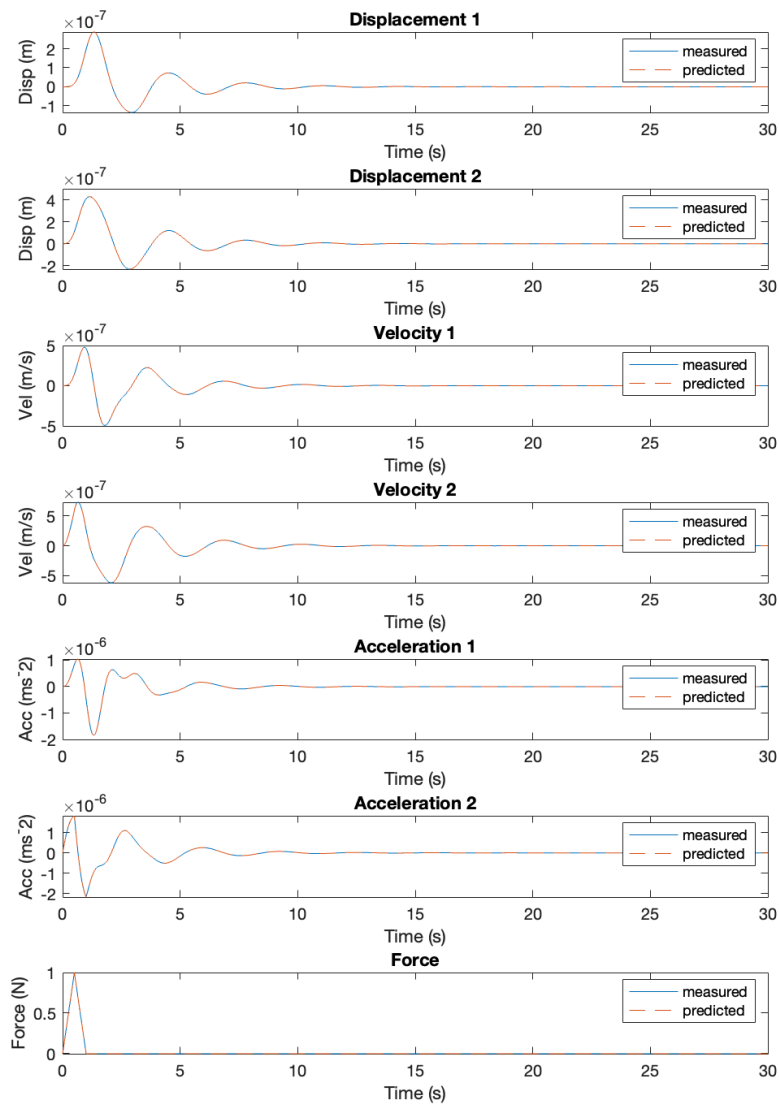


Figure 4.2: Time histories when all displacements, velocities and accelerations are measured

As expected, when all sensors are applied, the system exhibited a near-perfect oscillatory response

in displacement, velocity, and acceleration for approximately 15 seconds after a triangular pulse was applied at the second node.

Table 4.1 shows five different sensor setups and the resulting accuracy for each predicted displacement, velocities, accelerations and force. Displacement sensors and accelerometers are placed on m_1 and m_2 from Figure 4.1 in various combinations. The model's accuracy is assessed for each state using the coefficient of determination, also known as the R-squared value. The time histories of Cases D and E are shown in Figures 4.3 and 4.4, respectively. In Case D, only the system's displacements are measured, whereas in Case E, only the system's accelerations are measured.

Table 4.1: R-squared value for various sensor setups

Case	Sensors	x1	x2	v1	v2	a1	a2	F
A	disp 1, 2 and acc 1, 2	1.0000	1.0000	1.0000	1.0000	1.0000	1.0000	1.0000
B	disp 1, 2 and acc 2	1.0000	1.0000	1.0000	1.0000	1.0000	1.0000	1.0000
C	disp 1, 2 and acc 1	1.0000	1.0000	1.0000	1.0000	1.0000	0.9651	0.9632
D	disp 1, 2	1.0000	1.0000	1.0000	0.9877	0.9987	0.0028	0.0027
E	acc 1, 2	0.6626	0.5478	0.9999	0.9998	1.0000	1.0000	0.3909

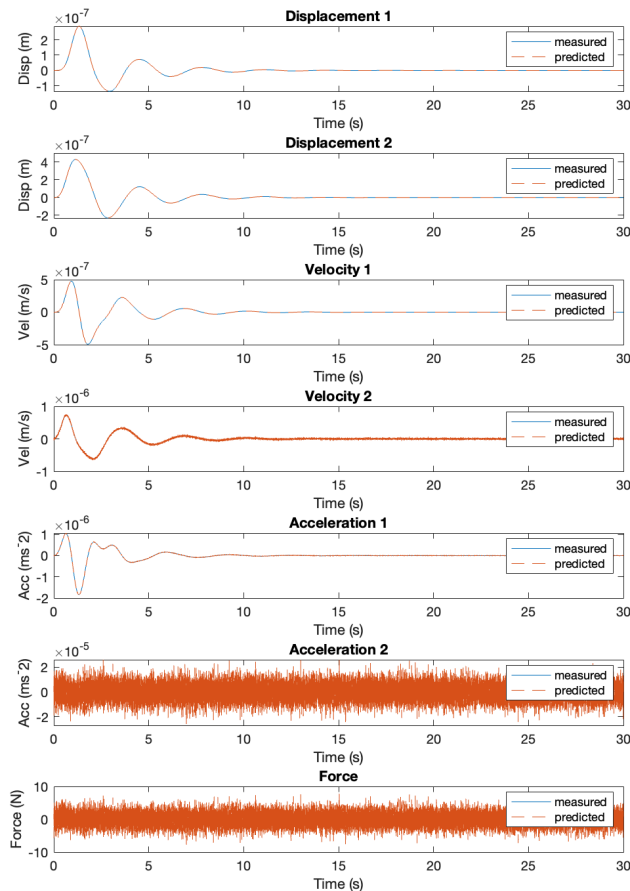


Figure 4.3: Time histories for Case D

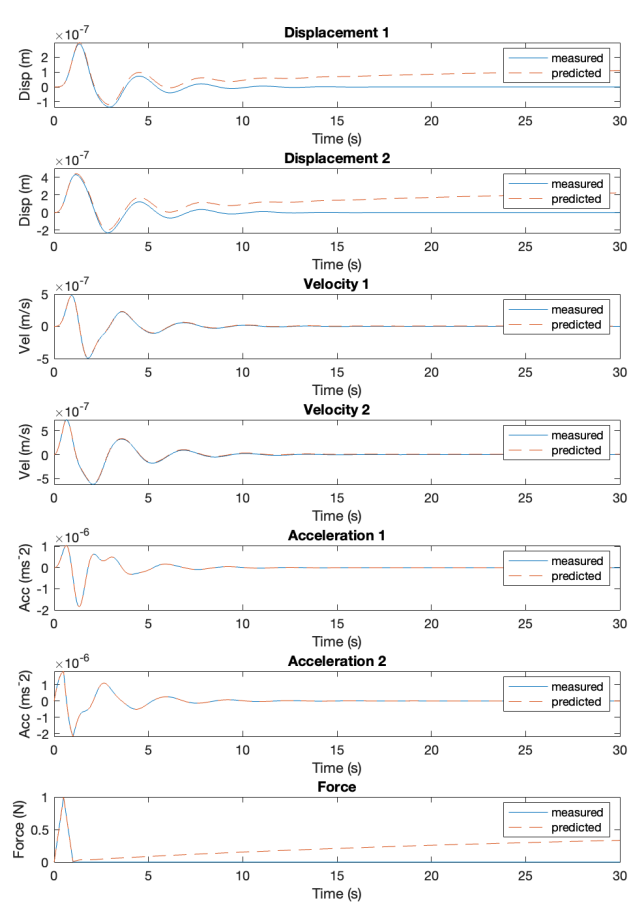


Figure 4.4: Time histories for Case E

When both nodes are fitted with displacement sensors and accelerometers, as in Case A, the predictions of all the states and the force are almost perfect. The time histories look almost identical to those shown in Figure 4.2. Table 4.1 shows that the predictions continue to be excellent when the accelerometer at the first node is removed, as in Case B. However, Case C shows that, when the second node accelerometer is removed, the force and acceleration predictions display some error because there is no collocation with the applied force. Table 4.1 illustrates that the R-squared value for the real and predicted force has decreased to 0.9632.

In Case D, when only displacements are measured, as shown in Figure 4.3, the displacements follow suit well, whereas acceleration and velocities have errors. The displacement is least related to acceleration and force states making the force almost impossible to predict. The velocity state predictions for Case E shown in Figure 4.4 exhibit an offset due to the unknown integration constant arising from the integration of the acceleration measurements. Indeed, as presented in Maes et al., this case would have been unobservable. Similarly, the displacement state predictions show a linear drift resulting from the integration constant. The presence of drifts in displacement and offsets in the velocity predictions can be attributed to the unobservability of direct measurements for these states. The unknown integration constants from the integration of acceleration measurements propagate into the velocity and displacement state predictions, leading to the observed discrepancies. Additional displacement sensors are necessary to make the problem observable.

It is possible to visualise the above results by considering the entries of the system matrices \mathbf{C} and \mathbf{D} (see Section 3.2.2), which connect the measured variables to the system states. The \mathbf{D} matrix must be non-zero to satisfy the condition of direct feedback. Therefore the accelerometer selection matrix \mathbf{S}_a must be non-zero.

$$\mathbf{C} = \begin{bmatrix} \mathbf{S}_d & \mathbf{0} \\ \mathbf{0} & \mathbf{S}_v \\ \mathbf{S}_a \mathbf{M}^{-1} \mathbf{K} & \mathbf{S}_a \mathbf{M}^{-1} \mathbf{C} \end{bmatrix}, \quad \mathbf{D} = \begin{bmatrix} \mathbf{0} \\ \mathbf{0} \\ \mathbf{S}_a \mathbf{M}^{-1} \end{bmatrix}, \quad (4.1)$$

For the MSD system used in this example, the acceleration for the second mode creates direct feedback for the force, so this acceleration must be measured to meet the collocation requirement for the AKF. When the acceleration at the second degree of freedom is not measured, the accuracy of the predicted force significantly declines, as seen in Case E.

Chapter 5

Wind Turbine Results

This chapter evaluates the accuracy and reliability of the AKF for estimating structural loads and stresses in offshore wind turbines. It explores various scenarios, defining the parameters used in the forward simulation for each subsection.

To begin, a reference scenario demonstrates the feasibility of using an AKF for estimating system dynamics in an untruncated model for which sensors are placed at all nodes above sea level. The forward simulation is evaluated in Subsection 5.2, examining the effect of modal truncation on the system's dynamic predictions. It is found that retaining four modes represents the system to a high degree of accuracy. Therefore, subsequent scenarios are evaluated using just four modes. Section 5.3 evaluates the impact of identification using the modal force rather than the physical force. Next, the identification results of applying the AKF to synthetic measurements are analysed. Various sensor setups are evaluated in Section 5.5, emphasising feasibility. The section identifies that an accelerometer and displacement sensor placed at 45m and 174.6m above the midline perform well, and the sensor configuration is thus chosen for further analysis. The offshore wind turbine is subjected to Kaimal wind and Jonswap wave loading. The ability of the AKF to identify system dynamics, stresses at the mudline, and fatigue life is considered for each loading case. Notably, it is discovered that inputs with a non-zero mean induces a shift in the system's predictions. Additionally, the analysis reveals that using only four modes for Kaimal wind loading creates fatigue life prediction with an accuracy of 1.9%. Finally, the results section considers the performance of the AKF for the realistic scenario where noise and uncertainty exist in the dynamic system. This investigation encompasses measurement noise and parameter uncertainties in the damping ratio, Young's modulus and soil stiffness. The AKF can react reasonably well to these uncertainties.

5.1 Reference Scenario

A reference scenario is established to evaluate the feasibility of utilising an AKF for predicting fatigue at the mudline. The sensor setup for this scenario is depicted in Figure 5.1, with displacement sensors

and accelerometers installed at all nodes along the tower between 45m and 174.6m. A Kaimal wind force is applied at the top of the tower (174.6m), and the resulting stresses are assessed at the mudline. Considering the challenges of underwater sensor installations, the sensors must be placed above sea level. A time history of the applied Kaimal load and the corresponding displacement can be found in Section 3.2.4.1. In this example, the system matrices used in OxDyn are the same as those used by the AKF, and there is no modal truncation. The resulting real and predicted stresses are compared in Figure 5.2.

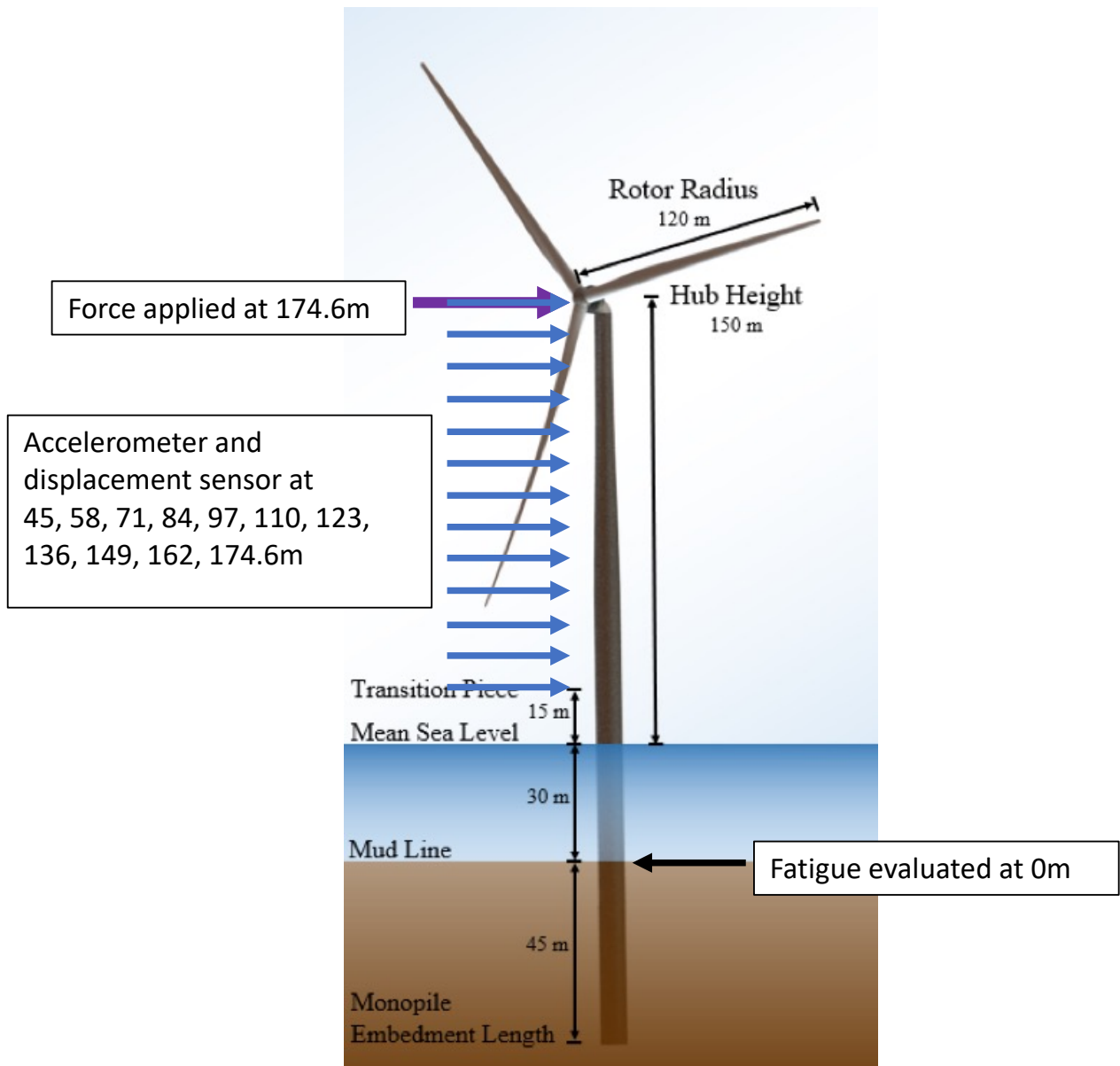


Figure 5.1: Sensor setup and fatigue analysis position

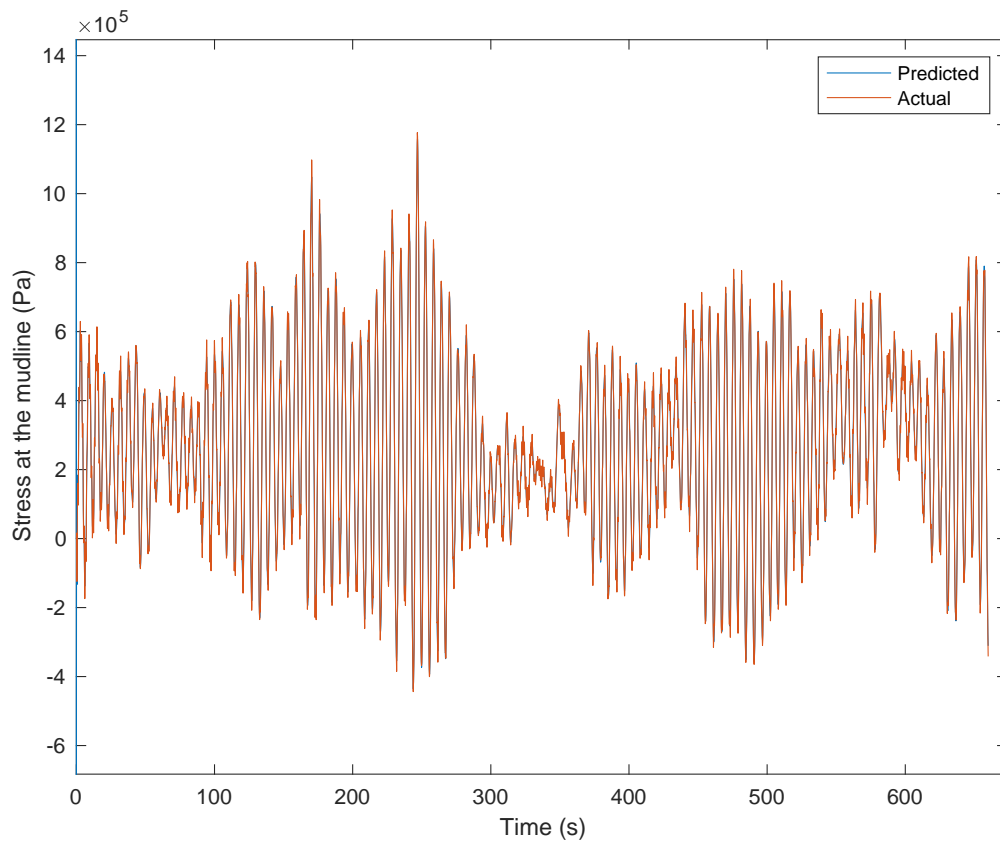


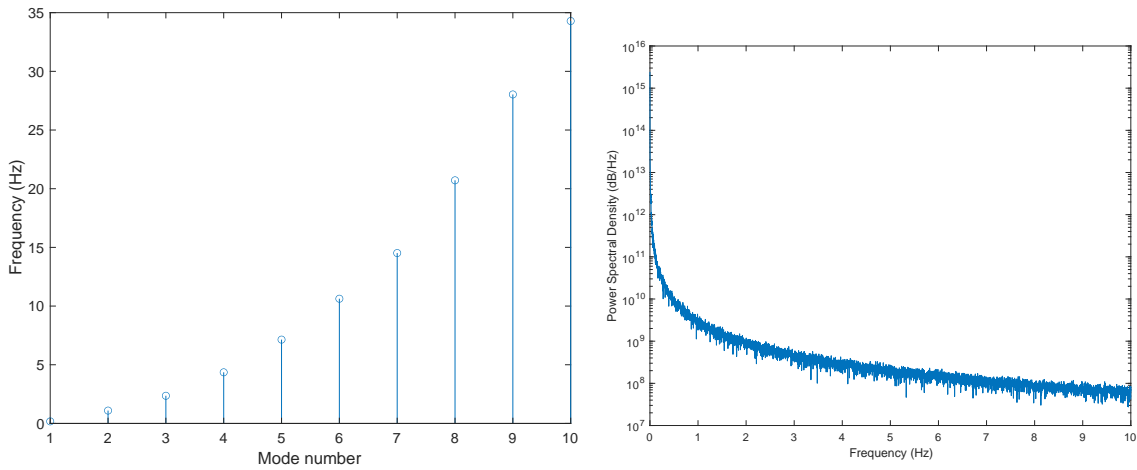
Figure 5.2: Stress at the mudline

The predicted stress levels at the mudline resemble the real stresses with a high degree of accuracy for this reference scenario, giving a good basis for testing other scenarios.

5.2 Modal Truncation

In the context of wind turbines, it is helpful to consider metrics that can provide insight into the input force's frequency content and impact on the system's response. The power spectral density (PSD) provides information about energy distribution across different frequencies and can reveal resonant frequencies that are particularly sensitive to the input signal. The impact of resonant frequencies on the system's response will depend on the excitation level at each frequency.

Figure 5.3(a) shows the first ten modal frequencies of the applied Kaimal wind and Figure 5.3(b) shows its PSD. The modeshapes of the first three modal frequencies are illustrated in Figure 5.4.



(a) First 10 modal frequencies of the wind turbine (b) Power spectral density of the applied Kaimal wind

Figure 5.3: System resonance frequencies and power spectral density of the input

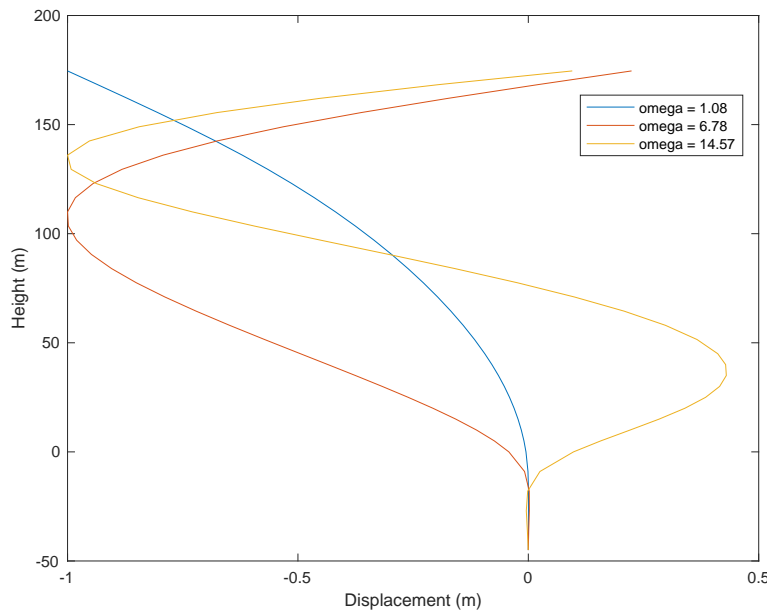


Figure 5.4: Modeshapes of the three lowest natural frequencies

It is clear from the PSD that the power of the applied Kaimal force experiences a sharp decline, dropping from around 10^{15} dB/Hz at 0 Hz to roughly 10^8 dB/Hz at 5 Hz. Therefore, four modes is a reasonable number of modes to capture the majority of the power. Modal truncation is a handy tool for creating real-time simulations of the wind turbine structure with faster processing times. For example, changing the number of modes in this system from 70 to 4 modes reduces the computational time of the AKF by a factor of 300, from 191.314 to 0.631 seconds.

OxDyn is used to calculate the complete wind turbine model and measurements. To show that a truncated model can accurately represent the system, the outputs from OxDyn can be compared with those from a truncated simulation, calculated in Section 3.2.2 and truncated as shown in Section 3.3.1. Table 5.1 shows the R-squared value between the full and truncated system for different numbers of

retained modes.

Table 5.1: R-squared value between the real and predicted displacement at the mudline for a modally truncated model with a varying number of retained modes

Number of retained modes	R-squared value
1	0.9770
2	0.9959
4	0.9972
6	0.9985
70	1

When all 70 modes are retained, Table 5.1 shows that the R-squared value is equal to one and the linear simulation perfectly aligns with the output of OxDyn. Each mode contains system information which is lost when truncated. However, the predicted displacement at the mudline is still accurate to 99.72% when only four modes are retained. All further scenarios will be evaluated using four modes due to the high accuracy. Figure 5.5 illustrates the system dynamics of both the full model, generated by OxDyn, and the truncated model, created using Matlab's `lsim()` function, applied to system matrices truncated to four modes.

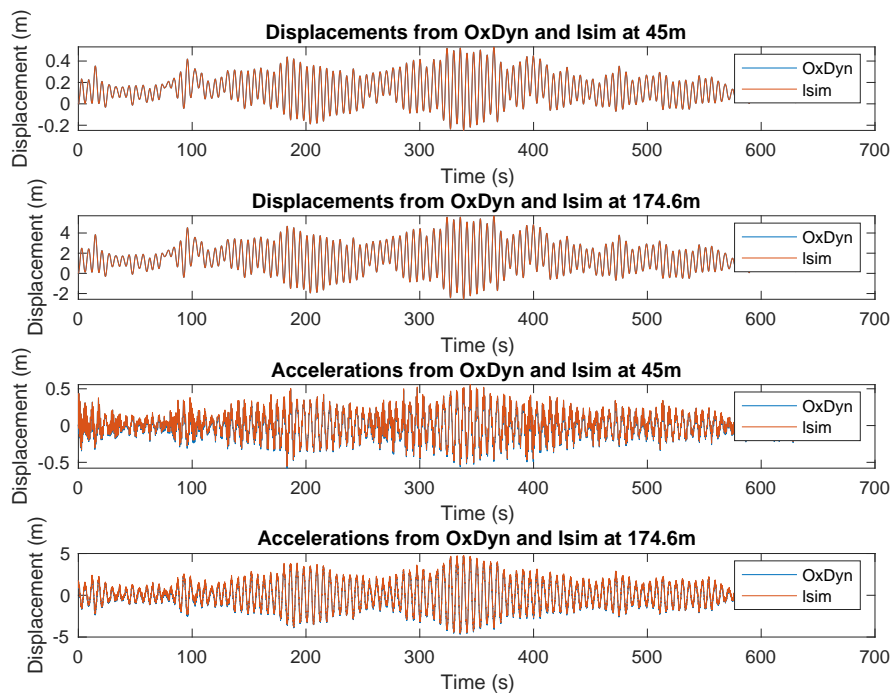


Figure 5.5: Displacements and accelerations of the full and truncated model using 4 modes

The truncated model generated with `lsim()` matches the full model closely. The displacements are almost identical, and there is a slight variation between accelerations. The similarity between the full and truncated system means that the underlying system matrices \mathbf{A} , \mathbf{B} , \mathbf{C} and \mathbf{D} used in the simulation are correct.

In terms of stiffness, when modal truncation is applied, the higher-order modes of vibration, which typically have smaller contributions to the system's dynamic response, are discarded from the model. This can lead to a reduction in stiffness in the remaining modes, particularly if the higher-order modes significantly contribute to the overall stiffness of the system.

5.3 Modal Forces

This section evaluates the use of modal and physical forces to estimate the input force for various process covariance noises.

It is possible to analyse the system in terms of modal forces using the equation $\mathbf{F}^*(t) = \mathbf{V}^T \mathbf{F}(t)$, as introduced in Section 3.3.1. The eigenvector matrix \mathbf{V} is truncated to the desired number of modes. Each modal force is included as a state to be estimated in the AKF. Therefore the modal force predictions are given as an output. Figure 5.6 shows an example of the time histories of the first four modes of a Kaimal wind load.

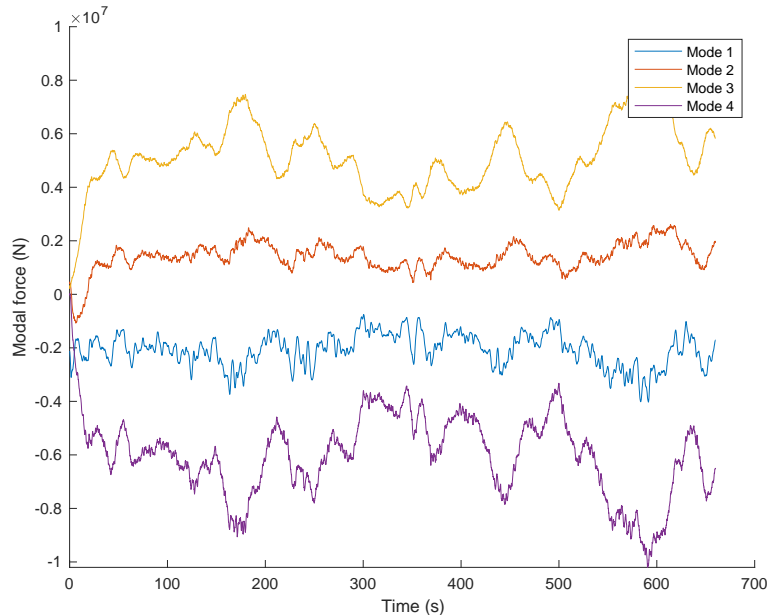


Figure 5.6: First four modal forces for a singly applied Kaimal wind load

To reconstruct the physical force, the inverse transformation is applied to the modal forces. This sums all the model forces shown in Figure 5.6 over their respective weighting factors. The modes relating to the smaller eigenvalues contribute more significantly to the overall dynamics dynamics.

Modal forces increase the number of unmeasured inputs to be estimated because a single physical

force is split into several modal forces that need to be identified. This increases the time taken to analyse the system. For example, when the number of force vectors to be estimated is changed from the single physical force to four modal forces, the computational time of the AKF for an 11-minute model is increased by around 22%, from 11.7s to 14.3s.

When using modal forces, there are two types of competing errors: the modelling error and the identification error. The impact of both sources of error can be assessed by varying the covariance matrices, which determine the AKF's weightings of the measurements and model, based on their respective reliabilities. The AKF's performance for estimating the input force using the physical and modal forces is evaluated for different process covariance noises in Table 5.2. Each table entry is evaluated for the same Kaimal wind load. Figure 5.3 shows the time history of the applied Kaimal force along with force predicted using the physical force and the modal forces, for a covariance noise of 10^{-5} , also represented by the second row of Table 5.2.

Table 5.2: R-squared values of the applied and predicted force for different process covariance noises estimating the physical and modal forces

Process covariance noise	Using the physical force	Using the modal forces
10^{-4}	0.4492	0.3702
10^{-5}	0.8033	0.7166
10^{-6}	0.9440	0.9039
10^{-8}	0.9827	0.9743
10^{-9}	0.9593	0.9743
10^{-12}	0.9282	0.9743

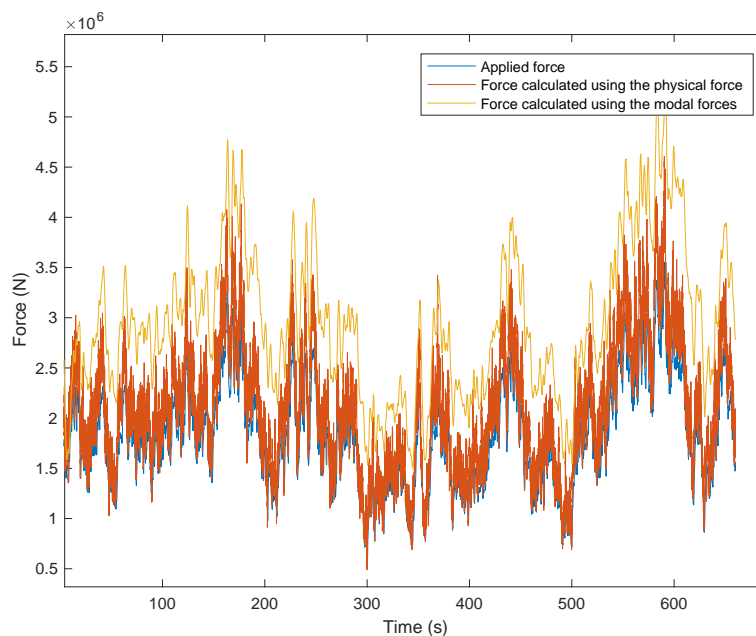


Figure 5.7: Comparison of applied and predicted force with a process covariance noise of 10^{-5}

Using modal forces to represent the model increases the identification error and reduces the modelling error. The identification error increases since the number of states that need to be identified at each step is higher for modal forces. A reduction in process noise corresponds to a decrease in the assumed uncertainty or randomness within the system that the model does not capture. By lowering the process noise covariance matrix, the AKF assigns less importance to the predicted state and more to the observed state. Table 5.2 shows that, for a process covariance noise greater than 10^{-8} , the AKF performance performs better when using the physical force than the modal force. This can be attributed to the fact that employing modal forces introduces added complexity due to the presence of additional states. Nonetheless, when the process covariance noise is sufficiently small, such as for 10^{-9} and 10^{-12} , the AKF effectively utilises the supplementary information provided by the modes, thereby making modal predictions more accurate. Improving the sensors' quality is one way to account for the additional detail required for modal force identification. For optimal results, the AKF must be informed via the process noise covariance of how precise the underlying model is, as explained in Section 3.4.1.

It is beneficial to use modal forces in real-life applications of force identification because modal forces are applied to all points along the structure, eliminating the requirement of physically collocating an accelerometer with the force for input identification. Consequently, direct feedback is established even when the accelerometer is not physically collocated with the applied force. Placing accelerometers at the exact load location can be challenging, particularly when dealing with wave loads below sea level. However, the mass matrix used to generate the system matrices in this system is not perfectly diagonal, as explored further in Section 5.5. This means that there is some direct feedback with the force for accelerometers placed at any node along the monopile. Therefore, in this example, the accelerometers must be placed far from the applied forces to observe the benefits that modal forces offer in terms of direct feedback.

The process noise covariance matrix captures the level of uncertainty in the system dynamics and the model and is essential for optimal performance of the AKF, with assumed prior knowledge of the process noise at each time step [36]. As shown in Table 5.2, increasing the number of modes without changing the covariance matrices does not improve the AKF's predictions, as the filter cannot incorporate the increased system precision.

5.4 Offset

Section 3.3.1 demonstrated how a simplified system version can be created by converting the system coordinates into modal coordinates and retaining only the lowest frequency terms. Figure 5.4 illustrates the predicted acceleration due to a unit step force for a full and truncated model.

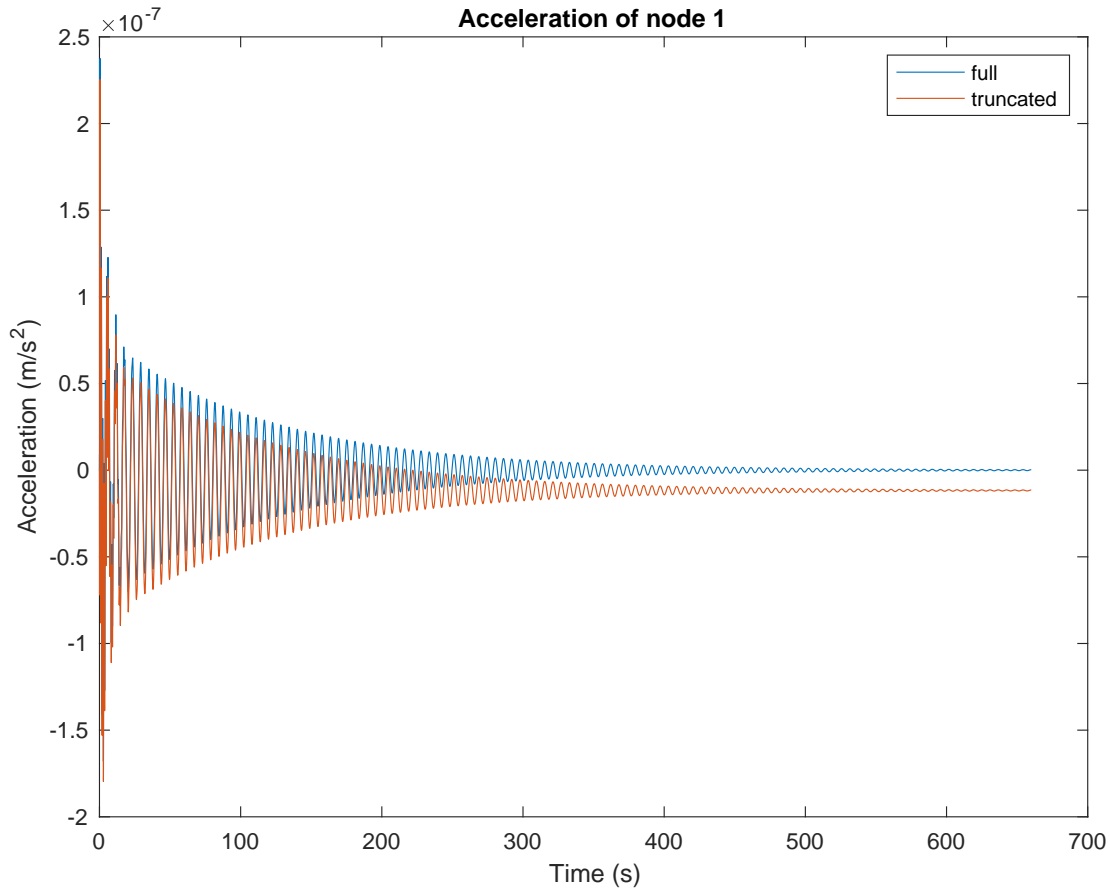


Figure 5.8: Comparison of the acceleration for the full and truncated model for a unit step force

The shift between the full and truncated model, observed in Figure 5.4, results from neglecting modal displacements with non-zero steady-state values. Due to this truncation process, the truncated model may not accurately reflect the forces applied to the system. A dummy variable can act as a substitute for a dependent variable in this situation where there is insufficient data available to counteract the truncation's effect on the steady-state forecasts [44].

In many real-world systems, wind loads typically have frequency components below 1Hz, as reported in [10]. Therefore, in such cases, band limiting the input force used in this model may be a viable approach to reduce the impact of truncation on system response while still capturing the realistic frequency components of the wind loading.

When running the program for various input loads such as a step force, white noise, Kaimal wind, and Jonswap noise, the amount of offset is directly proportional to the DC component of the input signal. In contrast, the system's dynamic response remains unaffected by this offset because omitting some modal displacements with non-zero steady-state values in the truncation process can result in deviations in predicted displacements and stresses, which we observe as an offset. Any bias in the force prediction causes a similar offset in the accelerations, which will bias the predictions. One way to account for the errors introduced by truncation is to increase the process noise, increasing

the uncertainty in the system. However, increasing the process noise too much can result in an overemphasis on the measurements and slow convergence and should therefore be done cautiously. Compared to the truncated model, the AKF can generate improved predictions for truncated systems by considering the inherent unreliability of the model. It achieves this by basing predictions on the true inputs rather than relying solely on the model.

5.5 Sensor Placement

In practice, placing high numbers of sensors on the turbine as in Section 5.1 is not feasible because the installation cost for a sensor along the tower can be estimated between \$1000 and \$2000 [32]. Therefore, this section focuses on determining an appropriate setup for a limited number of sensors. Because an AKF is used to create the predictions, the force input must have direct feedback for accurate force identification, as demonstrated in the example of the mass-spring-damper system in Section 4.

Table 5.3 shows several feasible sensor setups, where different combinations of displacement sensors and acceleration sensors are explored at heights 45, 71, 110 and 174.6m along the tower. The R-squared value of the real and predicted force is presented for each sensor setup. These results are obtained using four modes to reduce the computational time for each run, and the applied load is Kaimal wind at the top of the structure. The time history of the real and predicted forces for the first table entry (displacement sensor and accelerometer at 45 and 174.6m) is shown in Section 5.6.1.

Table 5.3: R-squared value for the real and predicted force for various sensor setups

Height of disp sensors (m)	Height of acc sensors (m)	R-squared value
45, 174.6	45, 174.6	0.9270
45, 174.6	45, 110	0.8811
45, 174.6	45	0.8530
None	174.6	0.7953
None	71	0.7069

The accuracy of the AKF predictions for wind force decreases as the accelerometer is moved further away from the force input because the collocation with the force decreases with distance.

When the second acceleration sensor is collocated with the force, the AKF predicts the force within 7.8% of the true value. However, as the sensors move further down the structure to 100m, the accuracy decreases and is worst when the second accelerometer is omitted entirely. The AKF necessitates a non-zero \mathbf{D} matrix, which signifies the direct influence of input forces on the measurements. For all cases, the AKF can still predict the force to some degree of accuracy, despite the lack of a physically collocated accelerometer. This is because the mass matrix used to create the \mathbf{J}_c and \mathbf{G}_c matrices is

not a perfectly diagonal matrix because the mass is distributed along the beam elements.

To simplify installation and maintenance processes, it is advisable to install displacement sensors and accelerometers at the same locations. From Table 5.3, the sensor setup with the most accurate force prediction is chosen for further analysis: a displacement sensor and accelerometer at heights 45m and 174.6m. This sensor configuration is used throughout the remainder of the report.

One of the sensor points is the nacelle position of 174.6m, where the wind load is applied, which allows for better direct feedback. The other sensor point is 45m above the mudline, at the transition point between the transition piece and the tower. Further benefit of taking measurements at 45m is that it is a key structural component that requires a greater emphasis on accuracy and is close to wave loads' location.

5.6 Loads Applied to the Wind Turbine

5.6.1 Kaimal wind analysis

Figure 5.9 shows the time history of the Kaimal wind input force and corresponding displacement at the height of 174.6m. Figure 5.10 compares the real and predicted forces and displacements at the height of 174.6m for Kaimal wind applied at the top of the structure. The sensors used in this analysis consisted of a displacement sensor and an accelerometer at 45m and 174.6m.

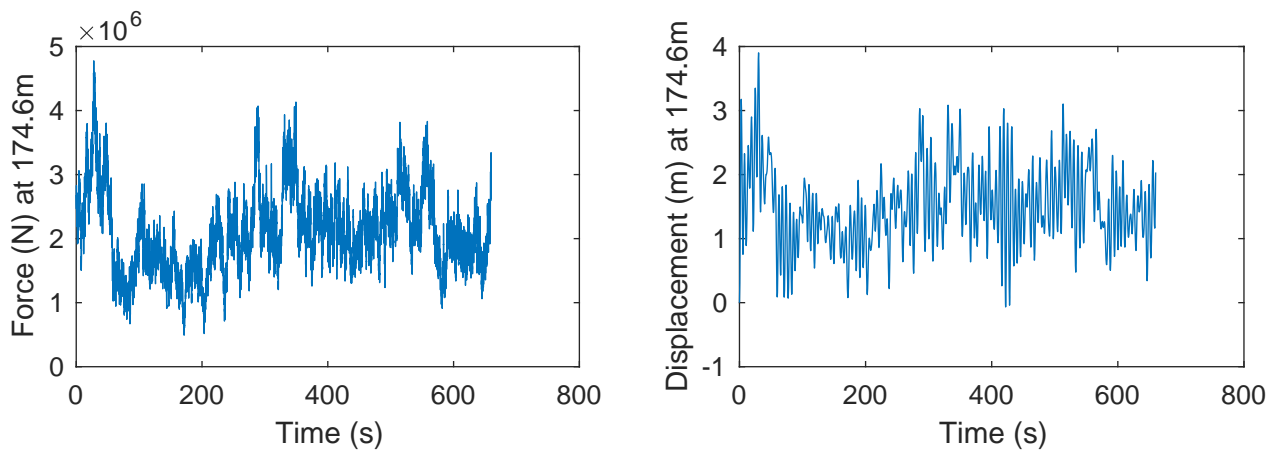
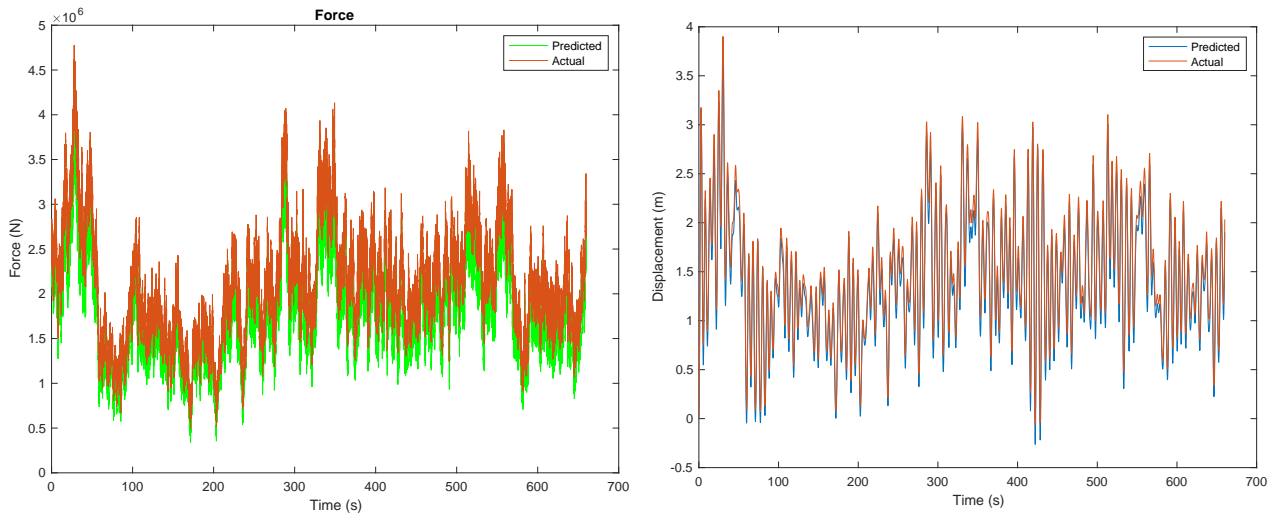


Figure 5.9: The Kaimal load (left) and the structure's displacement (right) at 174.6m



(a) Real and predicted force

(b) Real and predicted displacement

Figure 5.10: Response for Kaimal wind loading at 174.6m

Figure 5.10 shows that the predicted force and displacement follow the real dynamics very closely but with a constant vertical offset. This occurs because Kaimal wind is not zero mean, and a proportion of the steady-state response was lost in the truncation (see Section 3.3.1). The truncated model warrants adjusting the covariance matrices, increasing the process noise, and decreasing the measurement noise, thereby assigning greater weight to the measurements which have a high degree of accuracy. Although the AKF uses a truncated model, it benefits from the precise displacement and acceleration sensor inputs. As a result, the AKF attempts to address the inaccuracies arising from the modal truncation by introducing a slightly incorrect force. Consequently, the AKF's force identification for Kaimal wind is poor, as the filter compensates for the flawed model and preserves the accuracy of displacement and velocity sensors, a common occurrence in the field. Because only the displacements are utilised in the fatigue analysis, it is not critical that the predicted force is slightly inaccurate.

The AKF is able to identify the input force with an R-squared value of 0.9165, while the displacements have an R-squared correlation of 0.9992. These displacement values are to find the fatigue life estimate with an error of 2.05%. The majority of this difference is due to the offset caused by the truncation of the system. However, when an untruncated system model of 70 modes is used, the prediction error decreases to just 0.015%. For the untruncated system, the shift seen in Figure 5.6.1 reduced to almost zero, resulting in an R-squared value of 0.99 for the real and predicted force.

The real and predicted stresses, calculated from the displacements is shown in Figure 5.11

Using Equation 3.6.1 for Kaimal wind at a mean speed of 10.59 ms^{-1} the average mudline stress level comes to $1.3 \times 10^5 \text{ Pa}$. The AKF shows highly accurate estimates of the structure's fatigue damage with an error of only 1.9%. The real and predicted damage values over 11 minutes are 2.15×10^{14} and 2.11×10^{14} , respectively. Wind turbine structures are designed to last for a conservative duration

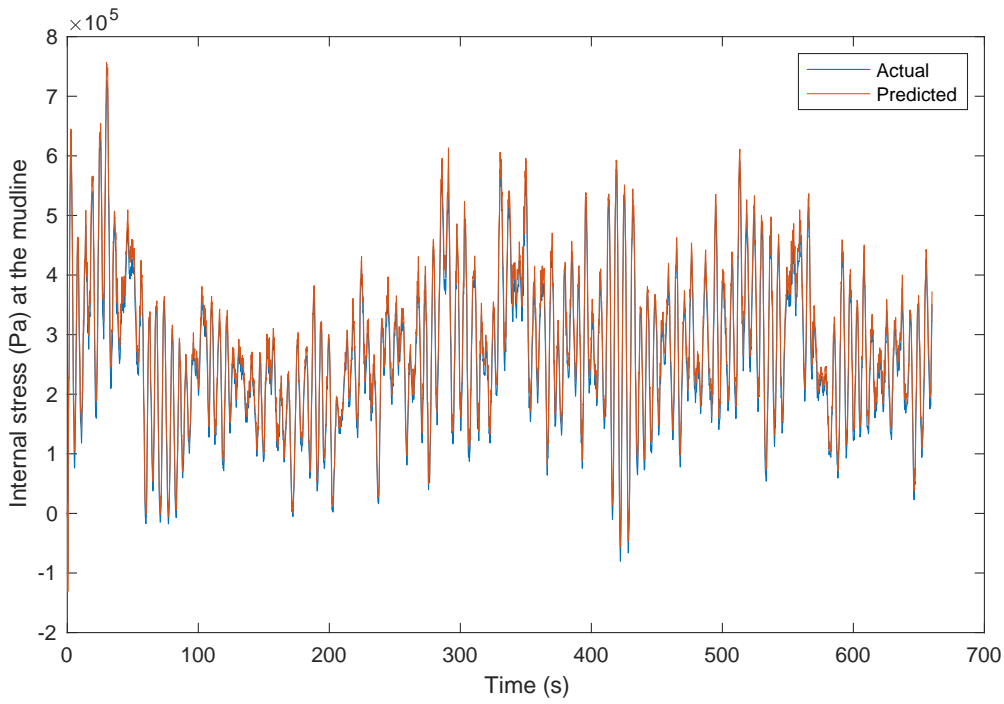


Figure 5.11: Real and predicted stress at the mudline for a Kaimal wind load

of 20-25 years and would experience minimal fatigue damage from this singularly applied wind load. Real wind turbines may have other loading sources, including wave loading and higher wind speeds. These loads can easily be incorporated into the AKF.

5.6.2 Jonswap wave analysis

To evaluate how the AKF’s performance for different loads and number of sensors, Jonswap wave loading is applied below the tower’s waterline, which creates several forces and moment inputs. Time histories of the Jonswap wave loading and displacement at the mudline are illustrated in Figure 5.12.

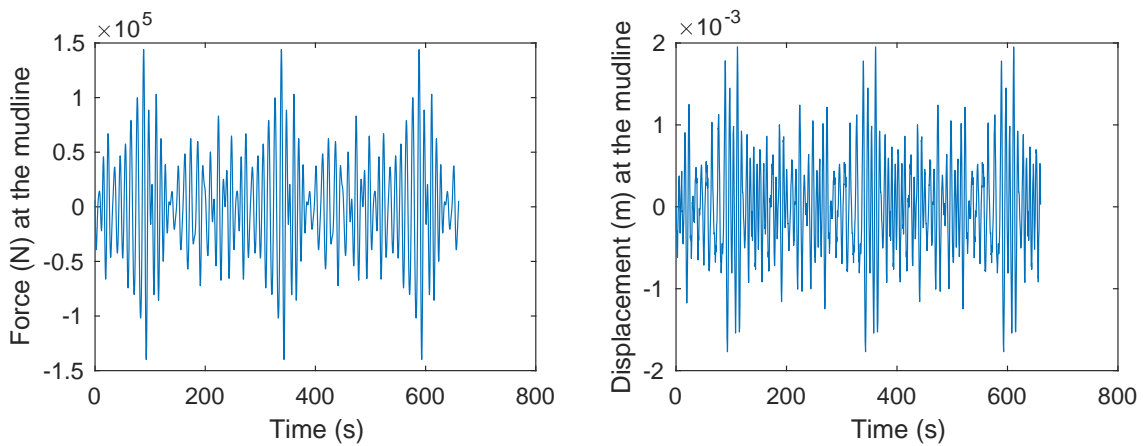


Figure 5.12: The Jonswap wave load (left) and the structure’s displacement (right) at the mudline

Figure 5.13(a) compares the real and predicted displacements for Jonswap loading at the mudline.

and Figure 5.13(b) shows the corresponding stress variation at the mudline.

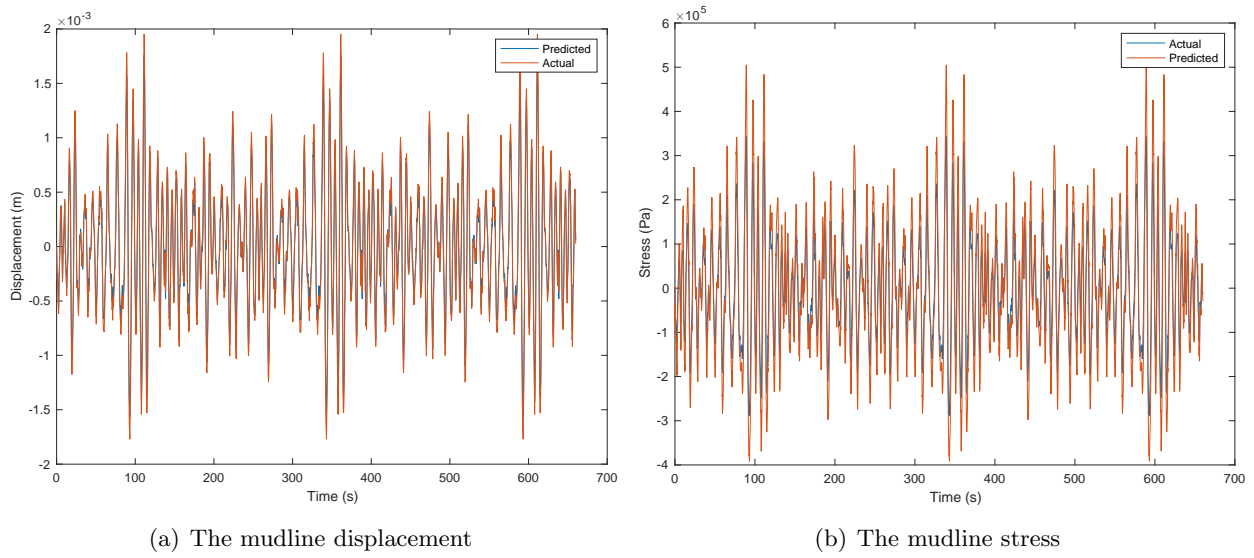


Figure 5.13: Response Jonswap wave loading

The AKF is able to follow the real displacement quite accurately, and there is no offset as for Jonswap wave loading because there is no steady state loading. However, introducing more force inputs increases the number of unknown parameters. Therefore, the overall system predictions are worse than before. It is possible to show this decrease in accuracy by evaluating the difference in the R-squared value between the predicted displacements at the mudline, which drops from 0.9779 for Kaimal wind to 0.9453 for Jonswap loading.

The real and predicted damage can be calculated from the stress time history shown in Figure 5.13(b). Part of the reason for the inaccurate Jonswap damage predictions is that Jonswap wave loading applies a force at every node between the mudline and the sea level. The wind turbine model has nine nodes below sea level, whereas only four sensors have been used in this analysis. However, to have an observable system, the number of sensors must equal or exceed the number of unknowns.

5.7 Noise and Uncertainties

There are many sources of uncertainties which could contribute to significant sources of error for off-shore wind turbines. For example, sensors transmit their measurements using electrical signals, which can be disturbed by Johnson noise and shot noise [38]. Johnson noise is caused by the random thermal motion of charge carriers in a conductor and is proportional to the temperature of the conductor. It can be reduced by cooling the conductor or by using low-noise amplifiers. Interference noise is caused by electromagnetic interference (EMI) from other devices or sources. It can be reduced by shielding the circuit or using filters to block unwanted frequencies. Environmental loads, such as the wind, mechanical components and wildlife, are unaccounted inputs which induce ambient vibrations in the structure. Moreover, some sensors may be less precise or even faulty, significantly distorting the

predictions. By measuring the coherence of the measurements, it is possible to account for incorrect sensor measurements in the AKF through their covariance.

In practice, measurements are never perfect due to noise, errors, and other sources of uncertainty. The AKF can be used to consider the uncertainty in the measurements by modelling the measurement noise as a Gaussian distribution with a mean of zero. The measurement covariance matrix describes the noise's statistical properties. The AKF requires the covariance noises to know how much to trust the sensors compared to the system. By incorporating information about the noise and uncertainty associated with the measurements taken by these sensors, the filter can produce more accurate and reliable estimates of these parameters than would be possible using the raw sensor data alone.

The effects of noisy measurements are incorporated into this system by adding a noise term to all measurements. For each data point of the dynamics, a value is chosen randomly from a standard normal distribution and then scaled by the noise root mean square (RMS) value. The ratio of noise RMS to signal RMS is varied between 0.01 and 0.1. The added noise simulates more realistic conditions to test the system's performance. Figure 5.14 shows the predicted force at 174.6m for the clean and noisy input data.

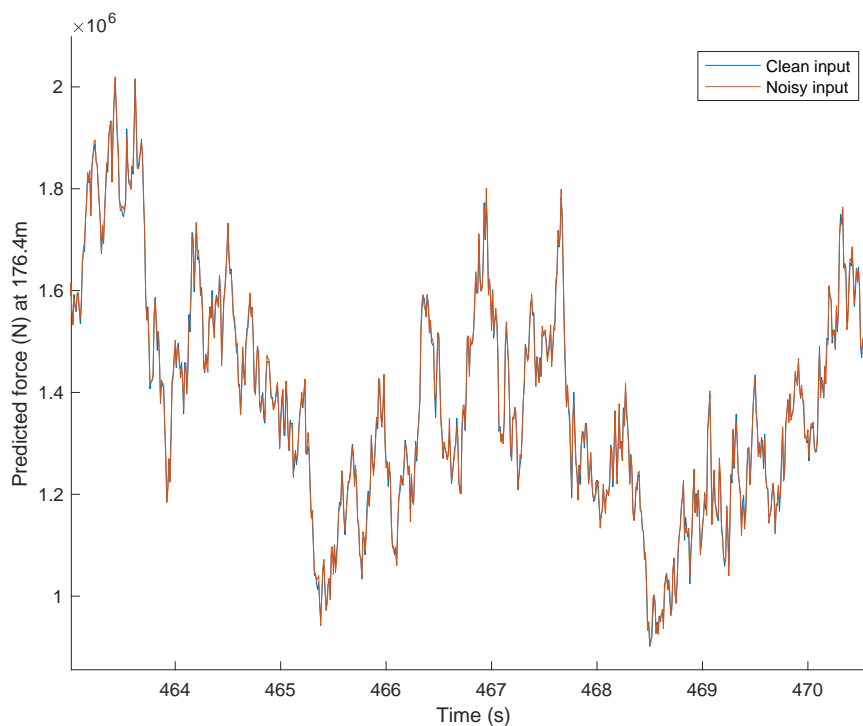


Figure 5.14: Predicted load for input data with and without a ratio of 0.01 rms noise to rms signal

There is a close resemblance for the predicted load using clean and noisy input data, meaning the AKF incorporates noisy data well by characterising the noise as an additional stochastic process. The force predictions for noisy and noiseless data are minimally different.

5.8 Parameter Uncertainties

In the current implementation of the AKF, the mass, stiffness, and damping matrices are assumed to be perfectly known and are obtained directly from the OxDyn wind turbine model. However, in real-world applications, various unknowns are associated with these parameters, making it necessary to account for these uncertainties in the AKF model. This section considers the effects of inaccuracies in the dynamic model and the impact of these uncertainties on the performance of the AKF. Evaluating the AKF under different conditions will allow us to understand the current approach's limitations better and develop strategies to improve the robustness and accuracy of the algorithm in real-world situations where the dynamic model is imperfect. Including model uncertainties is particularly important for offshore wind turbines, where complex interactions with hydrodynamic mass, soil, and other environmental factors can significantly affect the system's dynamics.

On-site, both the monopile's resonant frequencies and modeshapes are estimated. However, modeshapes estimations tend to be more challenging to identify. To assess the performance and robustness of this analysis under real-world conditions where the exact system model may not be available or accurate, the eigenvector is altered while maintaining similar resonant frequencies. This introduces a model error representing a practical scenario where incorrect foundation parameters and tower properties are used.

There are many methods to alter the eigenvectors of the model while maintaining similar resonant frequencies. One method is multiplying the displacements by a ramp, which gives similar frequencies but more base rotation and less steel flexure. In practice, the soil stiffness estimation has an uncertainty of about 10% and significantly contributes to the incorrect modes. To avoid violating the laws of physics, the eigenvalues can be altered by changing the system's physical parameters. By factoring up the steel's Young's modulus and factoring down the soil stiffness and the resulting stiffness matrix can be used to create the AKF system matrices **A**, **B**, **C**, and **D** defined in Section 3.2.2.

The aerodynamic drag of the turbine may occasionally give extremely high damping levels in the range of 5%. The wind-induced damping reduces the dynamic response of the structure to wave forces. This increased damping can have a negative influence on the AKF's performance. As damping increases, the duration of the transient response decreases, causing the system to reach a steady state more quickly. Moreover, future measurements are influenced less by the system's past behaviours, making it more challenging for the AKF to estimate inputs accurately.

5.8.1 Damping ratio

In this section, the accuracy of the AKF is evaluated for the situation when the real modal damping ratio of the wind turbine is 0.008 and the estimated structure damping ratio is different from the actual modal damping ratio. The time histories are most accurate when the damping prediction matches the real damping, creating an R-squared value of 0.9982 for the real and predicted system dynamics. The

predictions for estimated damping ratios of 0.007 and 0.009 are not as accurate but still reliable, giving R-squared values of 0.9682 and 0.9607, respectively. The R-squared values indicate that it is feasible to apply the AKF to real-world data where the system dynamics cannot be perfectly estimated.

Experimental values are obtained for varying damping ratios using each node's measurement covariance matrix (\mathbf{R}). This matrix is calculated by multiplying the root-mean-square (RMS) of the displacement by a factor. By decreasing this covariance noise, the AKF assigns greater importance to the highly accurate sensor measurements. As a result, with an inaccurate model, the stress estimations improve when using a smaller measurement noise covariance matrix. For instance, when the covariance matrix is equal to the measurement RMS multiplied by 10^{-6} , the stress estimations exhibit a 13% difference. In contrast, when the ' R ' matrix is scaled down by a factor of 100, the difference in stress estimations reduces to 7.2%.

5.8.2 Young's modulus and soil stiffness

In practice, it is challenging to obtain an accurate soil matrix. To account for the uncertainties in the soil, it is possible to scale the entire stiffness matrix. Similarly, the Young's modulus of the structure may be incorrect due to material variability and manufacturing defects. In order to alter the eigenvectors of the model while maintaining similar resonant frequencies, the AKF is run with incorrect state-space equations derived with only 70% of the soil stiffness and a 3% higher Young's modulus. This results in similar natural frequencies to the real system, as illustrated in Figure 5.15. Table 5.4 shows how varying the R covariance noise of the AKF influences the accuracy of the predicted damage.

Table 5.4: Damage fraction values for different covariance noises for an incorrect model

R covariance noise	Real damage	Predicted damage	Percentage difference
10^{-4}	2.15×10^{-14}	2.02×10^{-14}	6.05
10^{-8}	2.15×10^{-14}	2.18×10^{-14}	1.40
10^{-12}	2.15×10^{-14}	2.13×10^{-14}	0.93

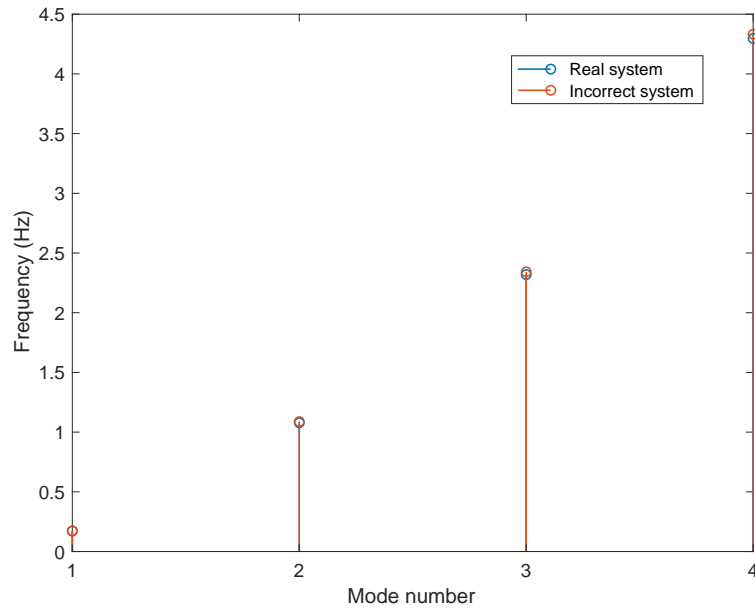


Figure 5.15: First 4 frequencies for the real and incorrect system

As depicted in Table 5.4, emphasising the measurements increases the prediction accuracy. This is because the synthetic measurements are much more reliable than the system in this example. Even for a covariance noise of 10^{-4} , the predicted damage is within 6.05% of the true value. However, in practice, if the R covariance noise value is too small, the filter may rely too much on the measurements, which, in turn, can lead to several issues, such as overconfidence in the measurements, slow convergence of the filter to the true state, and reduced robustness to measurement errors or outliers [43]. Nevertheless, in this specific example, the overfitting phenomenon is not observed because the applied noise is very small.

Chapter 6

Conclusion

6.1 Practical Conclusions

This report presents an in-depth study on implementing an augmented Kalman filter (AKF) to predict the structural dynamics, identify unmeasured forces and create a fatigue damage assessment of an offshore wind turbine. Utilising computational methods, including finite element analysis, to produce synthetic measurements, the AKF is applied to a realistic wind turbine model to evaluate its performance under various conditions. The AKF demonstrates promising capabilities in monitoring and maintaining offshore wind turbines by accurately predicting their structural dynamics, applied forces, and fatigue damage fraction. This approach can extend wind turbines' operational life, ensuring the renewable energy sector's sustained growth and success.

Several realistic subsets of sensors were evaluated for the wind turbine. Results are promising for two accelerometers and two displacement sensors placed at 45m and 174.6m along the wind turbine. This configuration enabled accurate system dynamics and fatigue damage predictions under various conditions. Section 4.2 emphasises the importance of direct feedback for identifying an applied force.

The noise sources, described in Section 5.7, were considered by incorporating noisy measurements into the system. The AKF produced highly accurate results using the covariance matrix \mathbf{Q} to account for the error. Uncertainties arising from unknown parameters such as soil stiffness, steel's Young's modulus, and damping ratio are analysed in Section 5.8, revealing that, in practice, it is better to use a smaller measurement noise and larger modelling noise to account for model errors arising from parameter uncertainty. The AKF proved robust in handling parameter uncertainty, with the system's accuracy only decreasing from 0.99 to 0.96 when considering a 10% damping uncertainty.

Truncating the model to reduce processing times resulted in an offset in the force caused by the removal of higher modes containing steady-state signals. The AKF produces an offset in the force to compensate for the system's inaccuracies and maintain accurate displacements. Therefore the structure's internal stresses can be estimated correctly despite the offset in force predictions.

The report successfully demonstrates that an AKF incorporating the augmented force state can predict the fatigue damage of an offshore wind turbine with a single applied load to an accuracy of 1.9%. Overall, this report successfully shows the feasibility of using an AKF to predict the fatigue life of a wind turbine system using limited sensors.

6.2 Recommendations for Further Work and Improvements

Although the study demonstrates promising results, it has several limitations and potential biases. For example, the damage values obtained in this study are lower than those of real wind turbines. Therefore a more comprehensive evaluation of environmental forces such as ocean currents, marine growth and storm surges would provide a better understanding of the AKF's performance in real-world conditions.

This report has described a specific sensor placement configuration that accurately predicts the wind turbine's structural dynamics and fatigue damage. However, the feasibility of precisely locating sensors at the specified positions on a real wind turbine may be limited by practical constraints, such as accessibility, installation challenges, or structural interference. A more detailed analysis of the sensor placement constraints and alternative configurations would provide valuable insights for implementing the AKF in real-world applications. Moreover, the same system matrices were used for generating synthetic measurements and evaluating the performance of the AKF. This approach may introduce a bias in the results, as the model's inherent assumptions and limitations could affect both the input data and the performance assessment. A more robust evaluation could be achieved by generating the data independently from the AKF.

An extension to the AKF is the simultaneous estimation of system parameters, such as stiffness and damping, in addition to the states and inputs. Given that the time evolution of the model's elasticity equals zero, the state space equations can be modified to incorporate the system parameters as additional states. This approach can enhance the overall performance of the AKF, particularly in cases where the system parameters are uncertain or subject to change over time. Batch inversion can also be employed to optimise the input estimates within the augmented Kalman filter (AKF). This method involves considering multiple inputs simultaneously and iteratively adjusting the input estimates based on metrics like the percentage difference between estimated and actual inputs. The goal is to minimise these differences and determine the optimal input estimates. Using batch inversion in combination with the AKF can improve the accuracy of the input-state estimations and better capture the system's behaviour, giving reasonable approximations for low levels of damping [27].

Bibliography

- [1] T. Adedipe and M. Shafiee. An economic assessment framework for decommissioning of offshore wind farms using a cost breakdown structure. *The International Journal of Life Cycle Assessment*, 26:1–27, 02 2021.
- [2] N. D. P. Barltrop and A. J. Adams. *Dynamics of fixed marine structures*, volume 91. Butterworth-Heinemann, 2013.
- [3] G. Bishop, G. Welch, et al. An introduction to the kalman filter. *Proc of SIGGRAPH, Course*, 8(27599-23175):41, 2001.
- [4] R. G. Brown and P. Y. C. Hwang. *Introduction to Random Signals and Applied Kalman Filtering with Matlab Exercises*. CourseSmart Series. Wiley, 2012.
- [5] H. J. Burd, D. M. G. Taborda, L. Zdravkovic, C. N. Abadie, B. W. Byrne, G. T. Houlsby, K. G. Gavin, D. J.P. Igoe, R. J. Jardine, C. M. Martin, R. A. McAdam, A. M. G. Pedro, and D. M. Potts. Pisa design model for monopiles for offshore wind turbines: Application to a marine sand. *Geotechnique*, 70:1048–1066, 11 2020.
- [6] B. W. Byrne, G. T. Houlsby, H. J. Burd, K. G. Gavin, D. J. P. Igoe, R. J. Jardine, C. M. Martin, R. A. McAdam, D. M. Potts, D. M. G. Taborda, et al. Pisa design model for monopiles for offshore wind turbines: application to a stiff glacial clay till. *Géotechnique*, 70(11):1030–1047, 2020.
- [7] C. C. Ciang, J. Lee, and H. Bang. Structural health monitoring for a wind turbine system: a review of damage detection methods. *Measurement Science and Technology*, 19(12):122001, 2008.
- [8] International Electrotechnical Commission. Wind energy generation systems-part 1: Design requirements. *International Electrotechnical Commission: Geneva, Switzerland*, 2019.
- [9] International Electrotechnical Commission et al. International standard wind energy generation systems–part 1: Design requirements, 2019.
- [10] I. Van der Hoven. Power spectrum of horizontal wind speed in the frequency range from 0.0007 to 900 cycles per hour. *Journal of Atmospheric Sciences*, 14(2):160 – 164, 1957.

- [11] V. K. Dertimanis, E. N. Chatzi, S. E. Azam, and C. Papadimitriou. Input-state-parameter estimation of structural systems from limited output information. *Mechanical Systems and Signal Processing*, 126:711–746, 2019.
- [12] DNV. Recommended practice-fatigue design of offshore steel structures. Technical report, DNVGL-RP-C203, 2019.
- [13] J. A. Fabunmi. Effects of structural modes on vibratory force determination by the pseudoinverse technique. *AIAA journal*, 24(3):504–509, 1986.
- [14] Z. Friedman and J. B. Kosmatka. An improved two-node timoshenko beam finite element. *Computers & structures*, 47(3):473–481, 1993.
- [15] E. Gaertner, J. Rinker, L. Sethuraman, F. Zahle, B. Anderson, G. E. Barter, N. J. Abbas, F. Meng, P. Bortolotti, and W. Skrzypinski. Iea wind tcp task 37: definition of the iea 15-megawatt offshore reference wind turbine. Technical report, National Renewable Energy, 2021.
- [16] National Grid Group. How much of the uk’s energy is renewable? <https://www.nationalgrid.com/stories/energy-explained/how-much-uks-energy-renewable>. Accessed: 2023-04-01.
- [17] K. Hasselmann, T. P. Barnett, E. Bouws, H. Carlson, D. E. Cartwright, K. Enke, J. A. Ewing, A. Gienapp, D. E. Hasselmann, P. Kruseman, et al. Measurements of wind-wave growth and swell decay during the joint north sea wave project (jonswap). *Ergaenzungsheft zur Deutschen Hydrographischen Zeitschrift, Reihe A*, 1973.
- [18] K. Hasselmann, T. P. Barnett, E. Bouws, H. Carlson, D. E. Cartwright, K. Enke, J. A. Ewing, A. Gienapp, D. E. Hasselmann, P. Kruseman, et al. Measurements of wind-wave growth and swell decay during the joint north sea wave project (jonswap). *Ergaenzungsheft zur Deutschen Hydrographischen Zeitschrift, Reihe A*, 1973.
- [19] M. Henkel, J. Häfele, W. Weijtjens, C. Devriendt, C. G. Gebhardt, and R. Rolfes. Strain estimation for offshore wind turbines with jacket substructures using dual-band modal expansion. *Marine Structures*, 71:102731, 2020.
- [20] R. Hermann and A. Krener. Nonlinear controllability and observability. *IEEE Transactions on Automatic Control*, 22(5):728–740, 1977.
- [21] IEC. Part 1: Design requirements, iec 61400-1. *International Electrotechnical Commission: Geneva, Switzerland*, 2005.
- [22] T. Ishihara and L. Wang. A study of modal damping for offshore wind turbines considering soil properties and foundation types. *Wind Energy*, 22:1760–1778, 12 2019.
- [23] J. C. Kaimal, J. C. Wyngaard, Y. Izumi, and O. R. Coté. Spectral characteristics of surface-layer turbulence. *Quarterly Journal of the Royal Meteorological Society*, 98:563–589, 7 1972.

- [24] R. E. Kalman. A New Approach to Linear Filtering and Prediction Problems. *Journal of Basic Engineering*, 82(1):35–45, 03 1960.
- [25] J. J. Kaulzarich. The palmgren-miner rule derived. In *Tribology Series*, volume 14, pages 175–179. Elsevier, 1989.
- [26] Y. Kumar, J. Ringenberg, S. S. Depuru, V. K. Devabhaktuni, J. W. Lee, E. Nikolaidis, B. Andersen, and A. Afjeh. Wind energy: Trends and enabling technologies. *Renewable and Sustainable Energy Reviews*, 53:209–224, 1 2016.
- [27] M. Liu and D. G. Gorman. Formulation of rayleigh damping and its extensions. *Computers and Structures*, 57:277–285, 10 1995.
- [28] E. Lourens, E. Reynders, G. De Roeck, G. Degrande, and G. Lombaert. An augmented kalman filter for force identification in structural dynamics. *Mechanical Systems and Signal Processing*, 27:446–460, 2 2012.
- [29] C. Ma, P. Tuan, D. Lin, and C. Liu. A study of an inverse method for the estimation of impulsive loads. *International journal of systems science*, 29(6):663–672, 1998.
- [30] K. Maes, M. N. Chatzis, and G. Lombaert. Observability of nonlinear systems with unmeasured inputs. *Mechanical Systems and Signal Processing*, 130:378–394, 2019.
- [31] R. McAdam. Oxdyn manual. *Oxford University Internal Reports*, 2022.
- [32] A. Mehrjoo, M. Song, B. Moaveni, C. Papadimitriou, and E. Hines. Optimal sensor placement for parameter estimation and virtual sensing of strains on an offshore wind turbine considering sensor installation cost. *Mechanical Systems and Signal Processing*, 169, 4 2022.
- [33] D. R. Mertz and M. A. Grubb. Steel bridge design handbook: Design for fatigue. Technical report, United States. Federal Highway Administration. Office of Bridge Technology, 2012.
- [34] L. Meyer, D. Ichalal, and V. Vigneron. An unknown input extended kalman filter for nonlinear stochastic systems. *European Journal of Control*, 56:51–61, 2020.
- [35] N. M. Newmark. A method of computation for structural dynamics. *Journal of the engineering mechanics division*, 85(3):67–94, 1959.
- [36] T. T. Ngoc, A. Khenchaf, and F. Comblet. Evaluating process and measurement noise in extended kalman filter for gnss position accuracy. In *2019 13th European Conference on Antennas and Propagation (EuCAP)*, pages 1–5, 2019.
- [37] L. J. L. Nordström. A dynamic programming algorithm for input estimation on linear time-variant systems. *Computer methods in applied mechanics and engineering*, 195(44-47):6407–6427, 2006.

- [38] D. V. Perepelitsa. Johnson noise and shot noise. *Department of Physics, MIT*, 2006.
- [39] L. Ramirez, D. Fraile, and G. Brindley. Offshore wind in europe: Key trends and statistics 2020, 2021.
- [40] M. I. Ribeiro. Kalman and extended kalman filters: Concept, derivation and properties. *Institute for Systems and Robotics*, 43(46):3736–3741, 2004.
- [41] S. Rodrigues, C. Restrepo, E. Kontos, R. T. Pinto, and P. Bauer. Trends of offshore wind projects. *Renewable and Sustainable Energy Reviews*, 49:1114–1135, 2015.
- [42] P. Schaumann, M. Boehm, and K. Schuermann. Improvements in the fatigue design of support structures for offshore wind turbines. *Steel Construction*, 14(2):74–82, 2021.
- [43] D. Simon. *Optimal state estimation: Kalman, H infinity, and nonlinear approaches*. John Wiley & Sons, 2006.
- [44] H. Tanizaki. Kalman filter model with qualitative dependent variables. *The Review of Economics and Statistics*, pages 747–752, 1993.
- [45] K. Tatsis and E. Lourens. A comparison of two kalman-type filters for robust extrapolation of offshore wind turbine support structure response. In *Life-Cycle of Engineering Systems*., pages 209–216. CRC Press, 2016.
- [46] P. Van der Male and E. Lourens. Estimation of accumulated fatigue damage in lattice support structures from operational vibrations. *Proceedings of EWEA Offshore, Copenhagen*, 2015.
- [47] S. Vanlanduit, P. Guillaume, B. Cauberghe, E. Parloo, G. De Sitter, and P. Verboven. On-line identification of operational loads using exogenous inputs. *Journal of Sound and Vibration*, 285(1-2):267–279, 2005.
- [48] E. A. Wan and R. van der Merwe. The unscented kalman filter. *Kalman Filtering and Neural Networks*, pages 221–280, 4 2003.
- [49] O. Zienkiewicz, R. Taylor, and J. Z. Zhu. The finite element method: its basis and fundamentals: Seventh edition. *The Finite Element Method: its Basis and Fundamentals: Seventh Edition*, pages 1–714, 2013.
- [50] J. Zou, E. Lourens, and A. Cicirello. Virtual sensing of subsoil strain response in monopile-based offshore wind turbines via gaussian process latent force models. *arXiv preprint arXiv:2207.05901*, 2022.